DIAGNOSTICS OF SUBSYNCHRONOUS VIBRATIONS IN ROTATING MACHINERY – METHODOLOGIES TO IDENTIFY POTENTIAL INSTABILITY

A Thesis

by

RAHUL KAR

Submitted to the Office of Graduate Studies of
Texas A&M University
in partial fulfillment of the requirements for the degree of

MASTER OF SCIENCE

August 2005

Major Subject: Mechanical Engineering

DIAGNOSTICS OF SUBSYNCHRONOUS VIBRATIONS IN ROTATING MACHINERY – METHODOLOGIES TO IDENTIFY POTENTIAL INSTABILITY

A Thesis

by

RAHUL KAR

Submitted to the Office of Graduate Studies of
Texas A&M University
in partial fulfillment of the requirements for the degree of

MASTER OF SCIENCE

Approved by:

Chair of Committee,	John M.Vance
Committee Members,	Alan Palazzolo
	Goong Chen
Head of Department,	Dennis O'Neal

August 2005

Major Subject: Mechanical Engineering

ABSTRACT

Diagnostics of Subsynchronous Vibrations in Rotating Machinery – Methodologies to Identify Potential Instability. (August 2005)

Rahul Kar, B.E., National Institute of Technology, India

Chair of Advisory Committee: Dr. John M.Vance

Rotordynamic instability can be disastrous for the operation of high speed turbomachinery in the industry. Most 'instabilities' are due to de-stabilizing cross coupled forces from variable fluid dynamic pressure around a rotor component, acting in the direction of the forward whirl and causing subsynchronous orbiting of the rotor. However, all subsynchronous whirling is not unstable and methods to diagnose the potentially unstable kind are critical to the health of the rotor-bearing system.

The objective of this thesis is to explore means of diagnosing whether subsynchronous vibrations are benign or have the potential to become unstable. Several methods will be detailed to draw lines of demarcation between the two. Considerable focus of the research has been on subharmonic vibrations induced from non-linear bearing stiffness and the study of vibration signals typical to such cases. An analytical model of a short-rigid rotor with stiffness non-linearity is used for numerical simulations and the results are verified with actual experiments.

Orbits filtered at the subsynchronous frequency are shown as a diagnostic tool to indicate benign vibrations as well as 'frequency tracking' and agreement of the

frequency with known eigenvalues. Several test rigs are utilized to practically demonstrate the above conclusions.

A remarkable finding has been the possibility of diagnosing instability using the synchronous phase angle. The synchronous phase angle β is the angle by which the unbalance vector leads the vibration vector. Experiments have proved that β changes appreciably when there is a de-stabilizing cross coupled force acting on the rotor as compared to when there is none. A special technique to calculate the change in β with cross-coupling is outlined along with empirical results to exemplify the case. Subsequently, a correlation between the synchronous phase angle and the phase angle measured with most industrial balancing instruments is derived so that the actual measurement of the true phase angle is not a necessity for diagnosis.

Requirements of advanced signal analysis techniques have led to the development of an extremely powerful rotordynamic measurement teststand – 'LVTRC'. The software was developed in tandem with this thesis project. It is a stand-alone application that can be used for field measurements and analysis by turbomachinery companies.

DEDICATION

To my Parents and Dr.Vance

"*It's a magical world, Hobbes, Ol' Buddy . . . let's go exploring!*"

- Bill Watterson

ACKNOWLEDGMENTS

I am indebted to Dr.Vance for the opportunity to conduct research at the Turbomachinery Laboratory. Without his deep insights and guidance this thesis would not have been possible. Mr. Preston Johnson (National Instruments) has been an inspiration behind the development of LVTRC – the ‘eyes’ and ‘ears’ of the research.

I am grateful to Dr. Palazzolo and Dr. Chen for consenting to oversee my thesis.

Special thanks are due to my friends and colleagues at the Turbomachinery Laboratory, especially to Mohsin Jafri for his analytical inputs, Bugra Ertas for helping me set up the test rigs and Kiran Toram for assisting with the experiments. Vivek Choudhury and Ahmed Gamal added definite spice to what has been two stimulating years at the laboratory.

The Turbomachinery Research Consortium has been kind enough to sponsor the research for two consecutive years.

Last but not the least, my parents have been outstanding in their support in every manner possible and this thesis is the outcome of their sacrifices.

TABLE OF CONTENTS

Page

CHAPTER Page

LIST OF FIGURES

Page

Page

Page

Page

CHAPTER I

INTRODUCTION

A serious problem affecting the reliability of modern day high speed turbomachinery is "rotordynamic instability" evidenced as subsynchronous whirl. The cause of instability is never unbalance in a rotor bearing system, but de-stabilizing cross coupled follower forces around the periphery of some rotor component. In mathematical terms (Lyapunov), "instability" is when the motion tends to increase without limit leading to destructive consequences. In most real cases, a "limit cycle" is reached, because the system parameters (stiffness/damping) do not remain linear with increasing amplitude. The rotor may then be operated at non-destructive amplitudes for years but needs rigorous monitoring tools, since any minor perturbation can destabilize the system and produce a rapid growth in amplitude. In the industry, large subsynchronous amplitudes are not a common occurrence, but are more destructive and difficult to remedy than imbalance problems when they do occur. Quite often, they are load or speed dependant, and build up to catastrophic levels under certain conditions.

Delineation based on definitions of critical speed and "instability" proves instructive. Vance [1] defines critical speed as the speed at which the response to unbalance is maximum. Instability is self-excited and is not dependent on the unbalance.

This thesis follows the style and format of Journal of Engineering for Gas Turbines and Power.

It is possible to pass through the critical speed of the machine without destruction, whereas a “threshold speed of instability” often cannot be exceeded without large-scale damage.

Mathematically, dynamic instability is the solution to homogenous linear differential equations of motion characterized by a complex eigenvalue with a positive real part. The real part is responsible for the exponential growth (or decay, if negative) of the solution while the imaginary part gives the damped frequency. From a rotordynamic viewpoint, the solution is the function which determines the time dependant amplitude of motion. A growing harmonic waveform is thus representative of instability as shown in Fig 1.

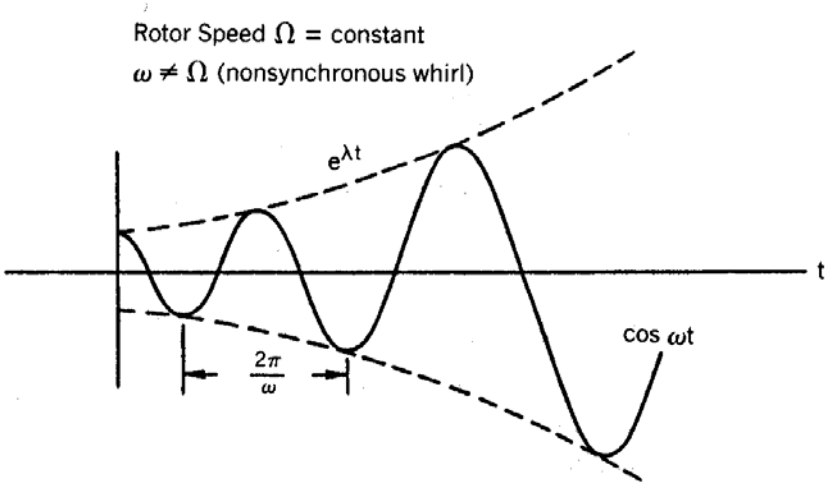

Fig 1: An unstable eigenvalue [1]

The factor in the differential equations that causes the vibration to grow is almost always cross-coupled stiffness, which models a force (usually from fluid pressure) driving the whirl orbit.

Lateral vibration signatures (periodic waveforms) captured with adequate transducers from a rotating machine represents the dynamic whirling motion of the rotor. Several signal analysis techniques can be used to extract pertinent information from these signatures – the Fast Fourier Transform (FFT) to obtain all the frequencies present in the signal, Bode plots for the synchronous rotor response, 'orbits' or Lissajous figures at filtered frequencies, accurate phase and magnitude values for all 'orders' etc. Analysis using these methods will make it possible to predict with a degree of certainty whether a rotor has the possibility of going unstable. The current research is to explore such methods and evaluate them with actual experiments at the Turbomachinery laboratory.

It is worth mentioning that existing rotordynamic measurement and signal analysis tools are not sufficient to extract significant information from subsynchronous signatures to aid in diagnostics. An advanced teststand with special algorithms is necessary for purposeful investigation.

Objective

The presence of benign subsynchronous vibrations from a rotor can easily be mistaken as instability, forcing the machine to be shut down out of fear of destruction. In a 1977 ASME paper [2], Ferrara at Nuovo Pignone examined whether subsynchronous vibration is a true indicator of incipient instability in high pressure multi-stage compressors. He studied two high-pressure compressors and concluded that some

asynchronous vibrations were the result of some "common cause" and was not self-excited. He recommended that the conventional criteria for determining possible instabilities should be re-evaluated.

The objective of this research is to study in detail, vibration signatures from benign and potentially unstable subsynchronous vibrations and find ways of differentiating between the two.

Literature Review

The occurrence of subsynchronous vibrations in rotating machines has been widely reported and documented. The first instances began to show up in the early 1920's when the need arose to operate rotors beyond the first critical speed. The following section is a brief review of research that has been done in this field.

The first published experimental observation of whirl induced instability was by Newkirk [3], in which he investigated nonsynchronous whirl in blast furnace compressors (GE) operating at supercritical speeds. He came to the conclusion that shaft whipping was because of internal friction from relative motion at the joint interfaces and not unbalance excitation. Kimball, working with Newkirk, built a test rig that demonstrated subsynchronous whirl due to internal friction in the rotating assembly. Newkirk also observed fluid bearing whip caused by the unequal pressure distribution about the journal. The enclosed fluid in the fluid film bearing clearance circulates with an average velocity equal to one-half the shaft speed [4]. Alford [5] hypothesized that tip clearances in axial flow turbines or compressors may induce non-synchronous whirling of the rotor. Den Hartog [6] described dry friction whip as an instability due to a

tangential Coulomb friction force acting opposite to the direction of shaft rotation (backward whirl). The tangential force will be proportional to the radial contact force between the journal and the bearing. Ehrich [7] has done a comprehensive survey of the possible causes of self-excited instabilities and suggested cures in most cases.

Ehrich [8] reported the occurrence of a large subsynchronous response at twice the critical speed from the analog computer simulation of a planar rotor model undergoing intermittent contact with the bearing surface. His 1966 paper has been discussed at greater length later in this thesis, since it has initiated the premise of research on subsynchronous rotor response due to bearing non-linearity. A similar phenomenon of "frequency demultiplication" is also presented by Den Hartog [6]. Bently [9] proposed and experimentally showed that subsynchronous rotor motion can originate from asymmetric clearances – "normal-tight' conditions when the rotor stiffness changes periodically on contact with a stationary surface or in "normal-loose" conditions when the radial stiffness changes (hydrodynamic bearings) during synchronous orbiting. Childs [10] solved non-linear differential equations describing a Jeffcott rotor to prove that ½ and 1/3 speed whirling occurs in rotors which are subject to periodic normal-loose or normal-tight radial stiffness variations. Vance [1] stated that rotordynamic instability is seldom from one particular cause and reviewed the mathematics for analyzing the stability of rotor-bearing systems through eigenvalue analysis. He also analyzed the case of supersynchronous instability or the 'gravity critical'. Wachel [11] presented several field problems with centrifugal compressors and steam turbines involving instability along with 'fixes' used to overcome the problems. A steam turbine was shown to have a

subsynchronous instability at 1800 rpm when the unit speed was 4800 rpm. The logarithmic decrement was found to be 0.04. The bearing length was reduced and the clearance increased so that the log-dec increased to 0.2. The subsynchronous instability disappeared. Another steam turbine case showed that changing to tilt-pad bearings was not sufficient to overcome one-half speed instability. The most difficult problem was instability in a gas re-injection compressor which suffered high vibration trip outs even before reaching operating speed. The subsynchronous frequency became higher than the first critical speed after modifying the oil seals. It was found that different seal designs greatly affected the non-synchronous frequency but did not make the unit stable. The stability improved greatly when a damper bearing was installed in series with the inboard bearing. The problem was mitigated by increasing the shaft diameter to raise the first critical speed and hence the onset speed of instability.

Research Procedure

A robust rotordynamic measurement teststand is required to signal-analyze subsynchronous vibrations. Currently available applications like ADRE from Bently Nevada are limited in their applications and will not be useful in the proposed research. For example, ADRE can only track subsynchronous frequencies in increments of 0.025 orders, which is extremely inflexible for extraction of data for a vibration which occurs at say, 0.470 orders. Consequently it was found necessary to develop a new rotordynamic measurement software solution (LVTRC) which exceed the capabilities of ADRE and help in diagnostics. LabVIEW from National Instruments was chosen as the software platform with which to develop the software, for its excellent graphical and

data acquisition capabilities. Two add-ons - the Order Analysis Toolset 2.0 and the Sound and Vibration Toolset, helped with advanced order extraction techniques and signal processing. Two 8-channel NI-4472 PCI boards were used for data acquisition and A/D conversion. Once the measurement teststand was in place, several test rigs were used to study known sources of benign and potentially unstable subsynchronous vibrations.

The exploration of the rotor response to non-linear bearing supports was of special interest. The method of investigation was based upon a paper by F.F Ehrich [8] claiming through analog computer simulations, that such a rotor would have a large subharmonic response at its first critical frequency when rotating at twice its critical speed (Fig 2 : Subharmonic response at the first critical speed [8].

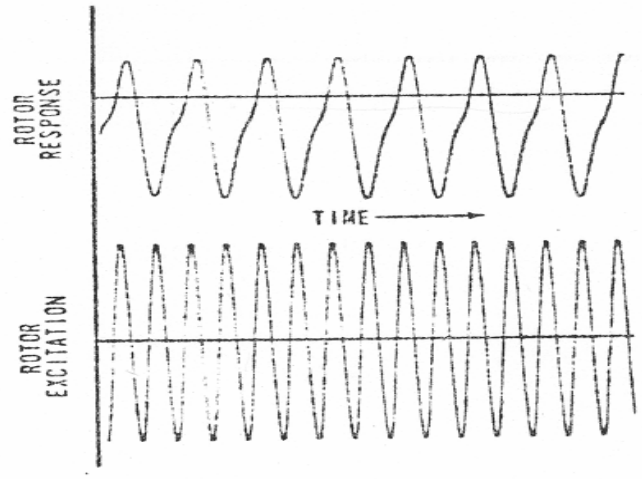

Fig 2 : Subharmonic response at the first critical speed [8]

The phenomenon was indeed found to occur in actual experiments and explained the often noted fact that “the onset of most asynchronous whirl phenomenon is at twice the induced whirl speed” [8].

A numerical rotordynamic model of a short rigid rotor undergoing intermittent contact with the bearing housing was developed so that its stiffness varied as a step function of the displacement along the direction of contact. The simulation results were compared with empirical data from a rig where non-linearity in bearing stiffness was artificially introduced.

Vibration signatures typical to instabilities were also studied at length especially from a rig where a forward acting de-stabilizing air swirl around the rotor could be turned on at will (a large subsynchronous vibration was induced at the first eigenvalue above the first critical speed).

It was also discovered that the synchronous phase angle (the angle by which the unbalance vector leads the vibration vector) was affected by destabilizing cross coupled forces. The change in phase angle from cross-coupling can be a remarkable tool for the diagnostics of subsynchronous vibrations in the industry

CHAPTER II

THE ROTORDYNAMIC MEASUREMENT TESTSTAND – 'LVTRC'

The Teststand

There are a number of differences between rotordynamics and structural vibrations that make measurement and diagnostics more difficult for rotordynamics. Examples are the occurrence of subsynchronous vibrations at fractions of the synchronous speed, the use of Lissajous patterns (orbits) with tachometer marks, the necessity of 'runout' subtraction from shaft vibration measurements and extracting accurate magnitude and phase information for different 'orders' of the running speed. The difficulties are also compounded by inflexible and limited data analysis systems currently available like the Bently Nevada ADRE™. Consequently, a new system has been developed using LabVIEW from National Instruments along with associated state-of-the-art data acquisition devices, to overcome most shortcomings and to enable advanced subsynchronous vibration study. A description of the teststand follows.

The teststand (Fig 3) is an Intel Pentium 4, 1.7 GHz personal computer with Windows®NT operating system, 512 MB RAM and 40 GB of hard drive space. The system is equipped with two NI 4472 PCI 8-channel boards for data acquisition and analysis. LabVIEW 7.0 Express with the Order Analysis 2.0 and Sound and Vibration Toolset is installed for programming and signal processing.

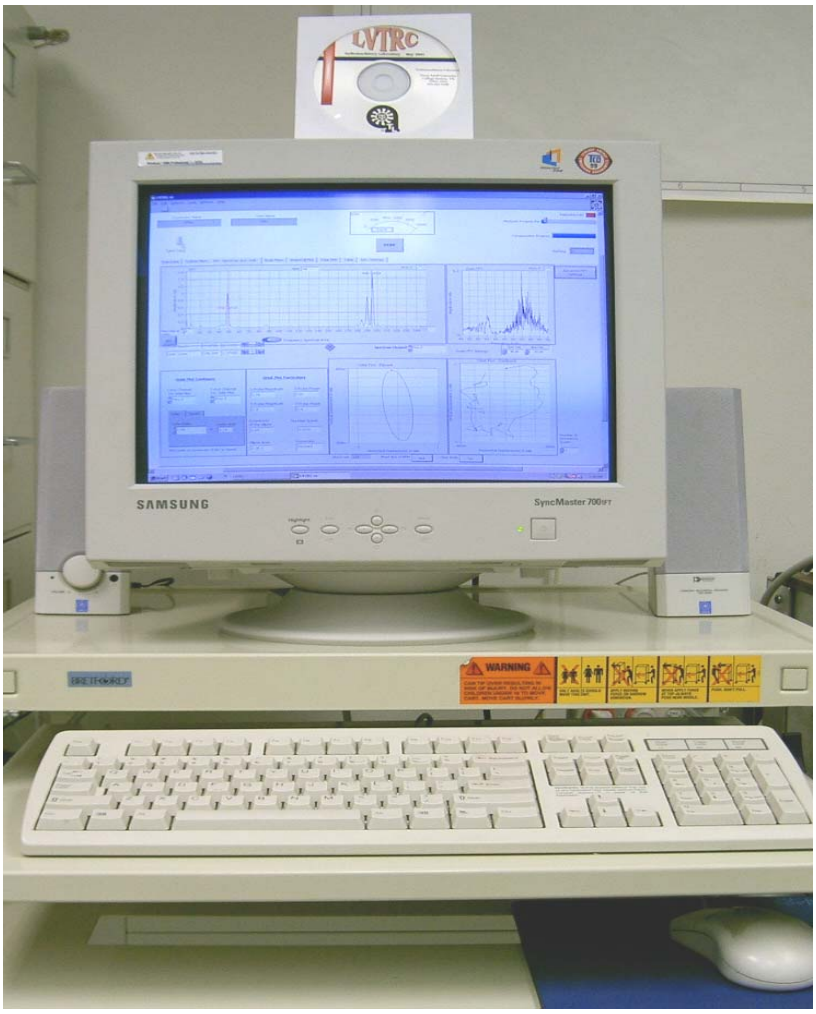

Fig 3: The LVTRC teststand

Proximity probes from Bently Nevada, powered by a -24V power supply are used for all measurements. The probes are connected to the data acquisition boards via NI attenuation cables to increase the acceptable voltage range from the input and run the application DC coupled.

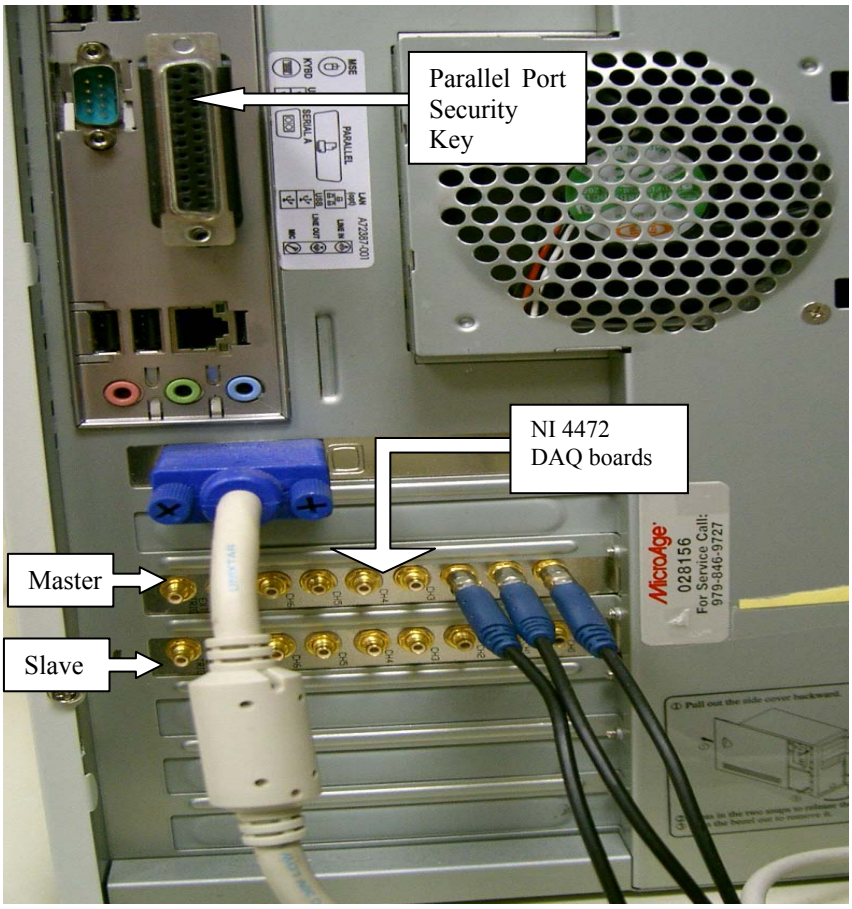

Fig 4: Three channels of input into the NI 4472 DAQ device

Test Setup

All measurements for experiments mentioned in this thesis were carried out using eddy current proximity probes. The probes were calibrated and set at a voltage gap of negative 8.0 V DC to ensure linear behavior. The 'leads' from the proximity probes were connected using BNC cables to the DAQ boards as shown in Fig 4. A schematic of the connection basics is shown in Fig 5.

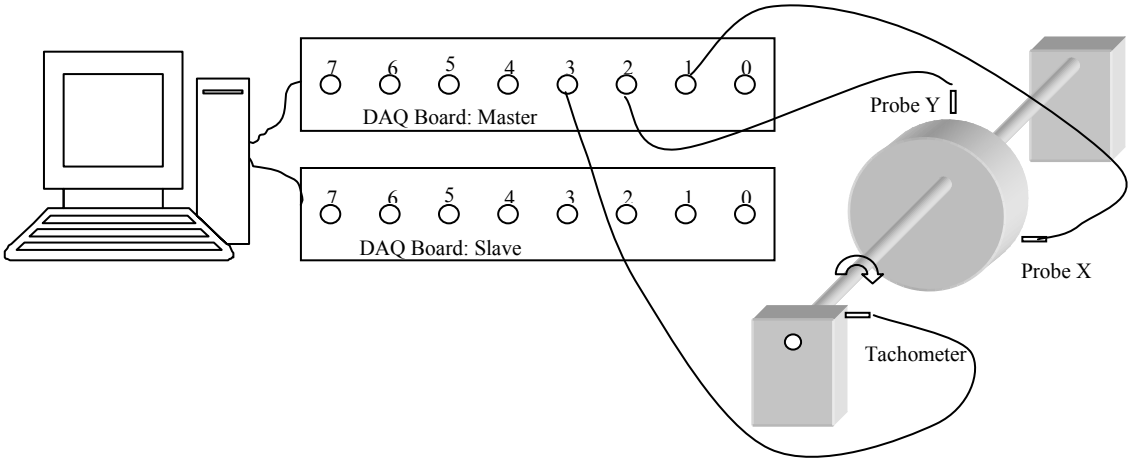

Fig 5: Experimental setup illustrating wire connections from the probes to individual pins of the DAQ boards

The channels have to be configured using the calibration units, probe orientation and whether to operate in AC or DC coupled mode.

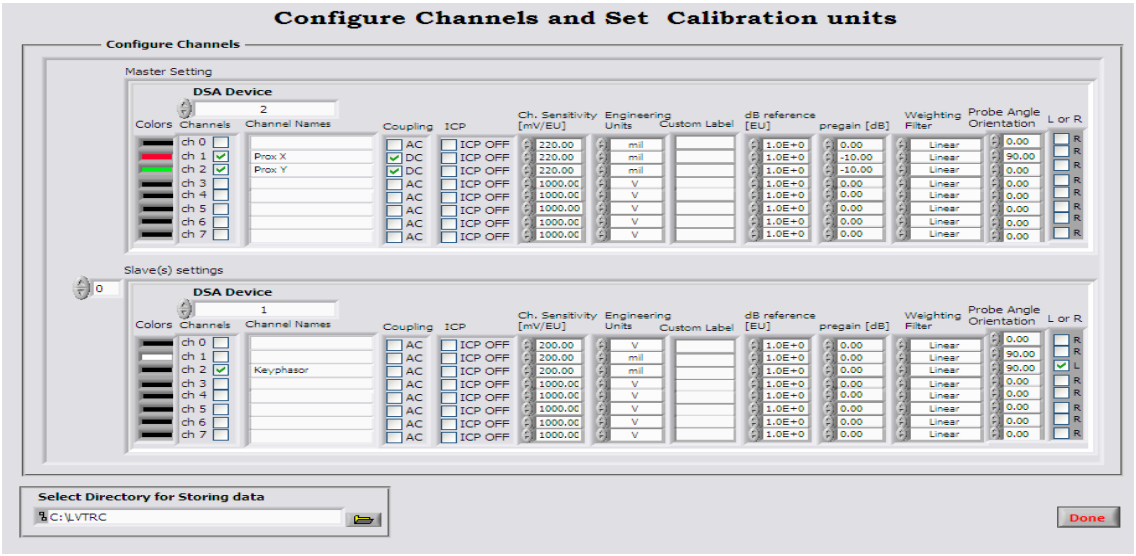

Fig 6: LVTRC channel configuration screen

Functional Blocks

The LVTRC application incorporates most functional blocks, which a standard rotordynamic data acquisition system has. The capabilities are briefly discussed below.

Time Series Data

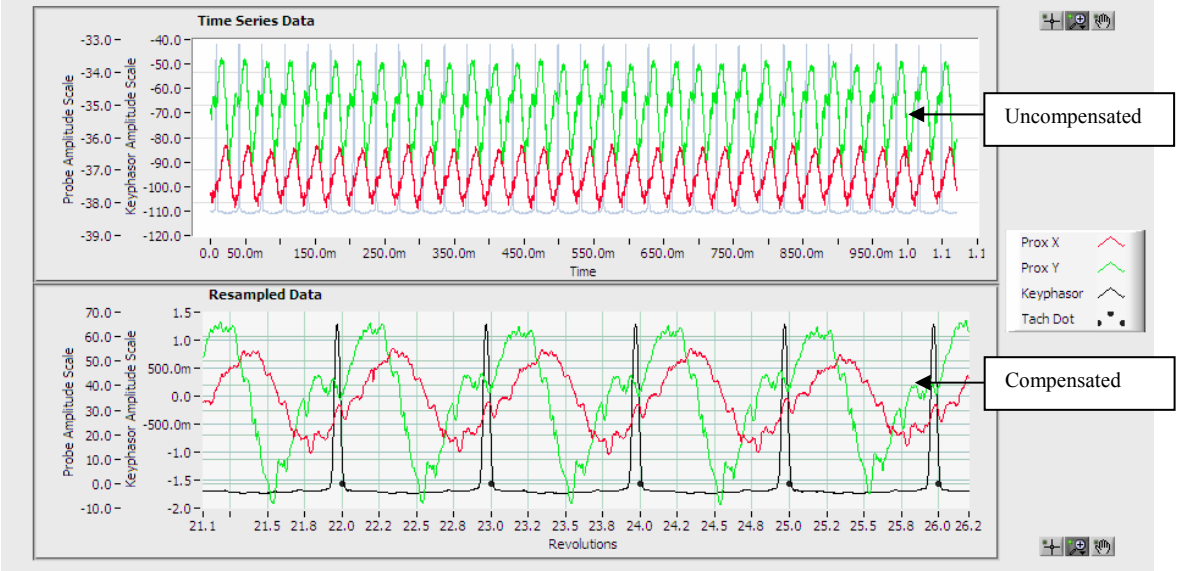

Fig 7: Time series and resampled-compensated data

Fig 7 shows the time series data captured from two proximity probes and a tachometer. The first graph is the raw voltage signal converted to engineering units (in this case mils) while the second plot is resampled data, compensated and with the DC component subtracted. Resampling changes the data from the time domain to the angular domain.

Spectrum and Orbit

Malfunctions in rotating machines (loose ball bearings, shaft misalignment, rubs, instabilities etc) leave tell-tale stamps on the spectrum and orbit plots, in terms of the fraction of the running speeds they occur, the tendency to track the synchronous component, the ellipticity of the orbit (Fig 8) etc. LVTRC has advanced tracking filters which can extract accurate phase and magnitude information for any 'order' of the running speed.

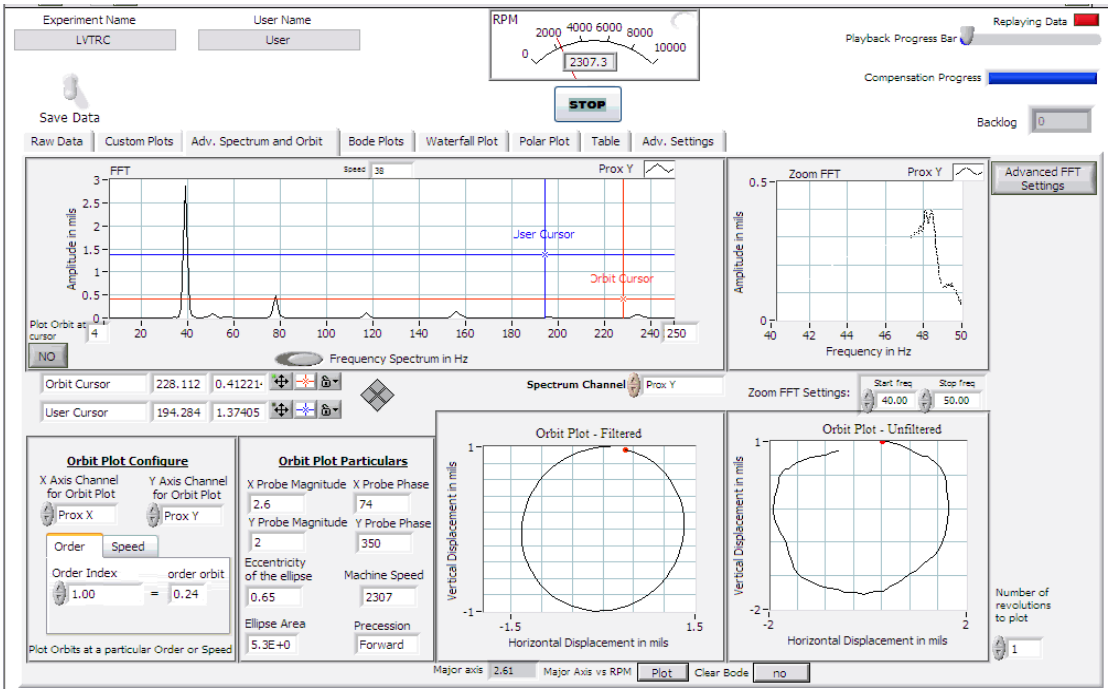

Fig 8: Spectrum and orbit plots

One of the most useful features of the application is the ability to plot orbits exactly at frequencies where the user places his/her cursor on the Spectrum plot (Fig 9).

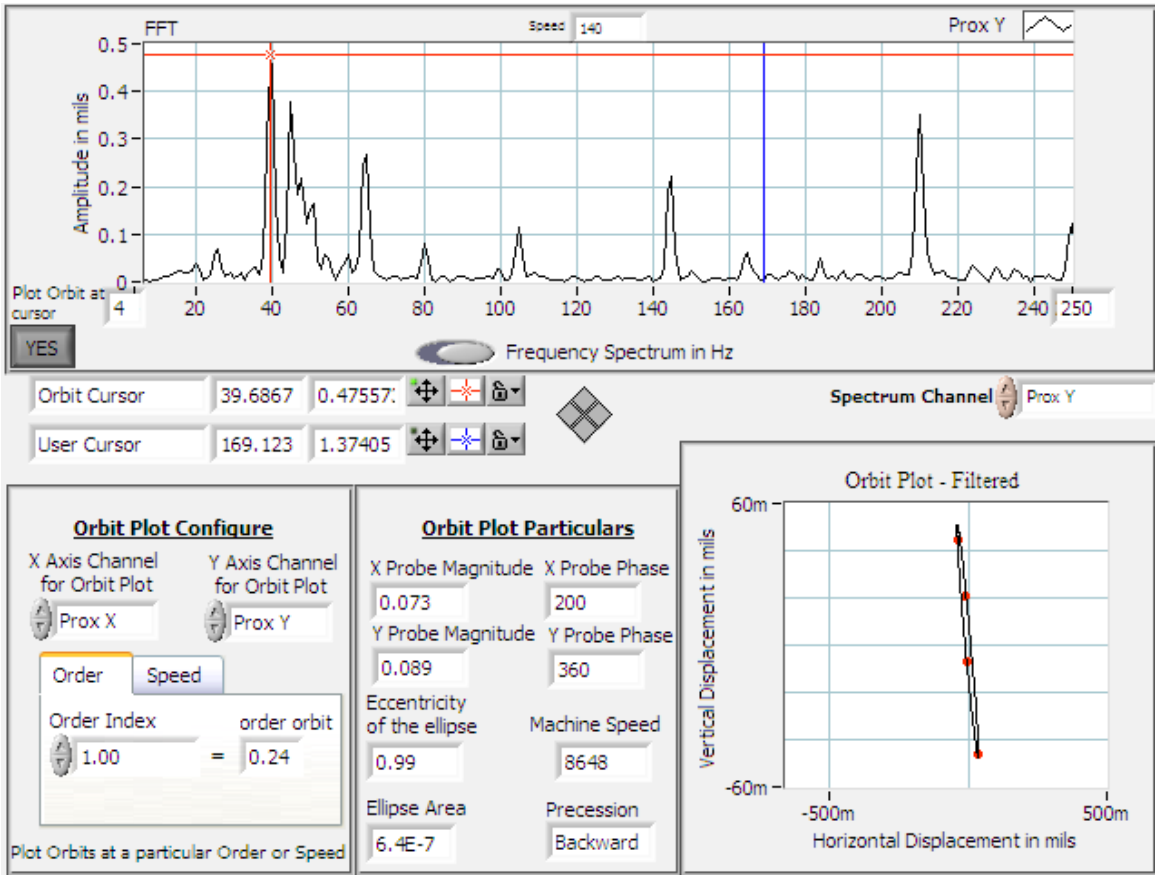

Fig 9: Cursor driven orbit

The red cursor is placed at the 40 Hz component on the frequency spectrum. The orbit at that frequency is plotted. This feature will be used in the study of how orbits filtered at a particular subsynchronous frequency behave when the rotor is potentially unstable.

Bode Plots

Bode plots (Fig 10) illustrate the rotor response (amplitude and phase) to changing rotor speed. LVTRC maintains buffered Bode plot data from the raw signals; so that any channel and any order can be selected at any point of the experiment and the full history of the rotor response may be obtained.

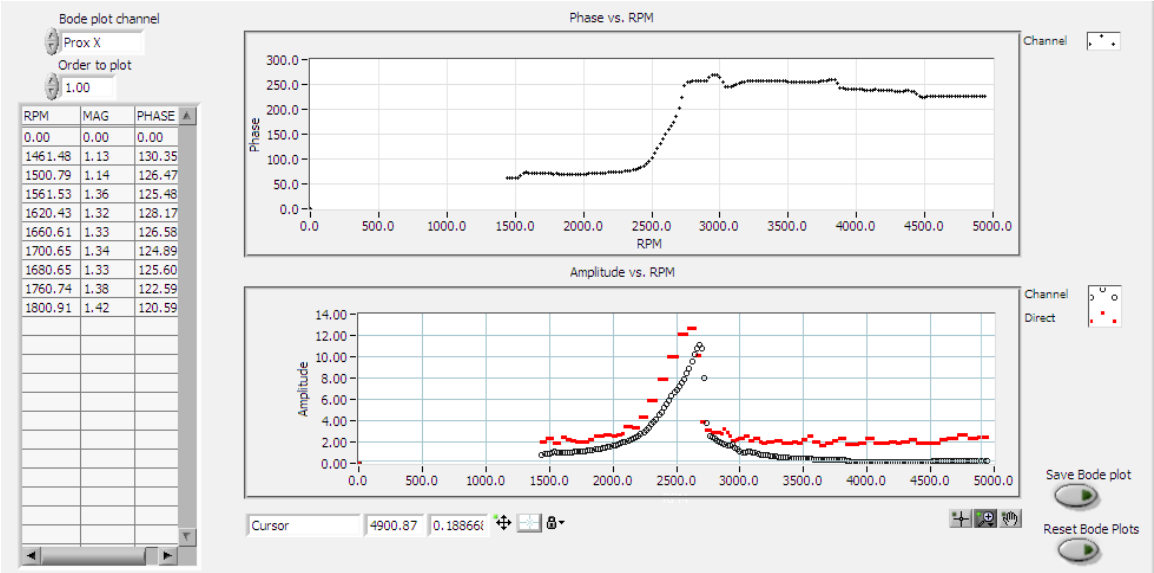

Fig 10: Bode plot

Waterfall Plot

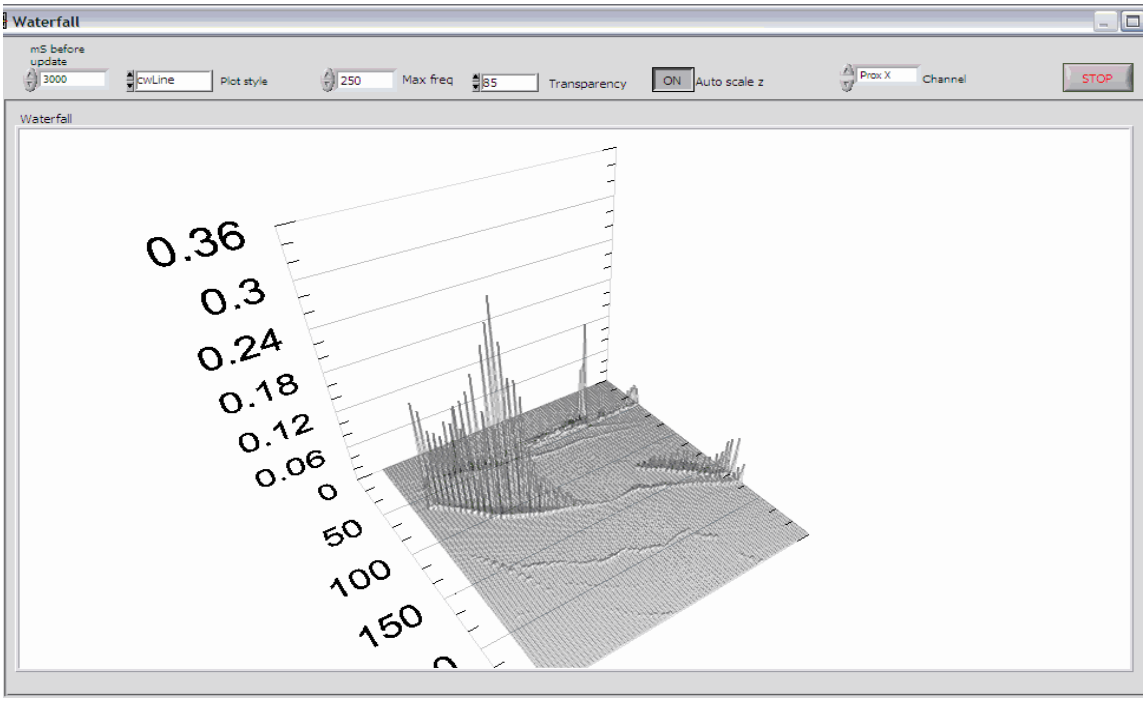

Fig 11: Waterfall plot obtained from a proximity probe

Several of the features like the waterfall plot (Fig 11) have been used extensively to obtain very encouraging results. The detailed development of the code is not discussed here as it is beyond the scope of this thesis.

CHAPTER III

SUBHARMONIC VIBRATION OF ROTORS IN BEARING CLEARANCE

Review of F.F.Ehrich's 1966 ASME Paper [8]

Ehrich's paper describes subsynchronous whirl generated due to non-linearity in rotor stiffness and uses analog computer simulation to show that "the excitation at the second harmonic induces a large component of first-harmonic response. It is suggested that this subharmonic resonance or frequency demultiplication may play a large role in the often noted fact that the onset of most asynchronous whirl phenomenon is at twice the induced whirl speed". The interest of this thesis originates from the idea that any non-linearity in stiffness of the rotor-bearing system (the source is immaterial) will produce a large subsynchronous response when running at twice the critical speed and can be easily mistaken for an instability.

Clearances between the rotor and stator in a high-speed rotating system lead to non-linear spring stiffness. The static equilibrium position of the rotor may not be at the bearing center (Fig 12) but may be eccentric and be in contact with one side of the bearing (Fig 13). Another and perhaps more realistic case is the intermittent contact between the journal and the bearing due to rotor vibration (Fig 14).

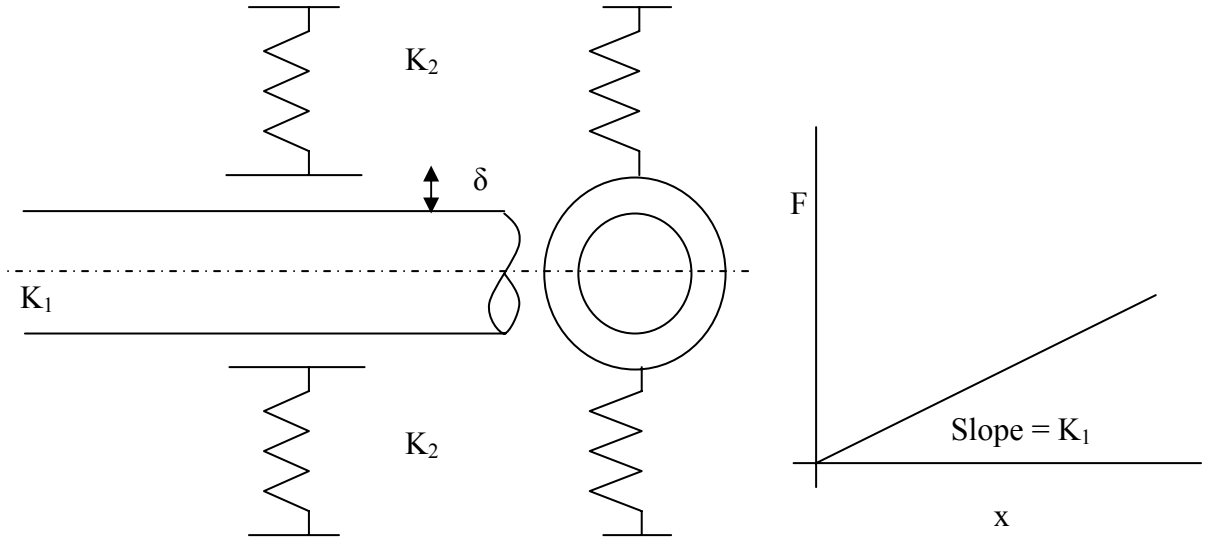

Fig 12: Rotor at bearing center

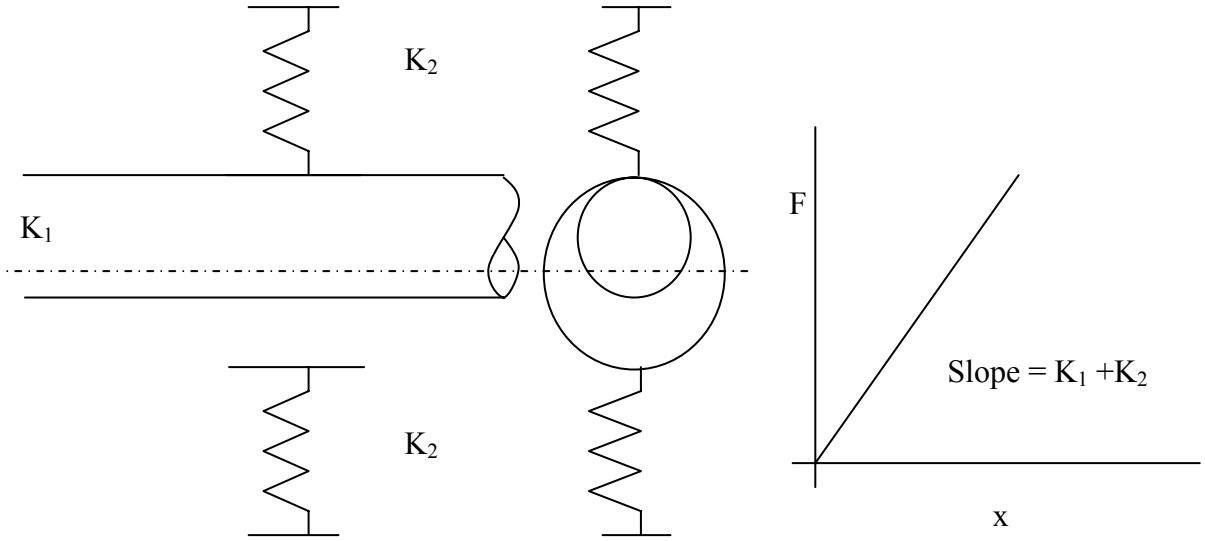

Fig 13: Rotor in constant contact with the stator

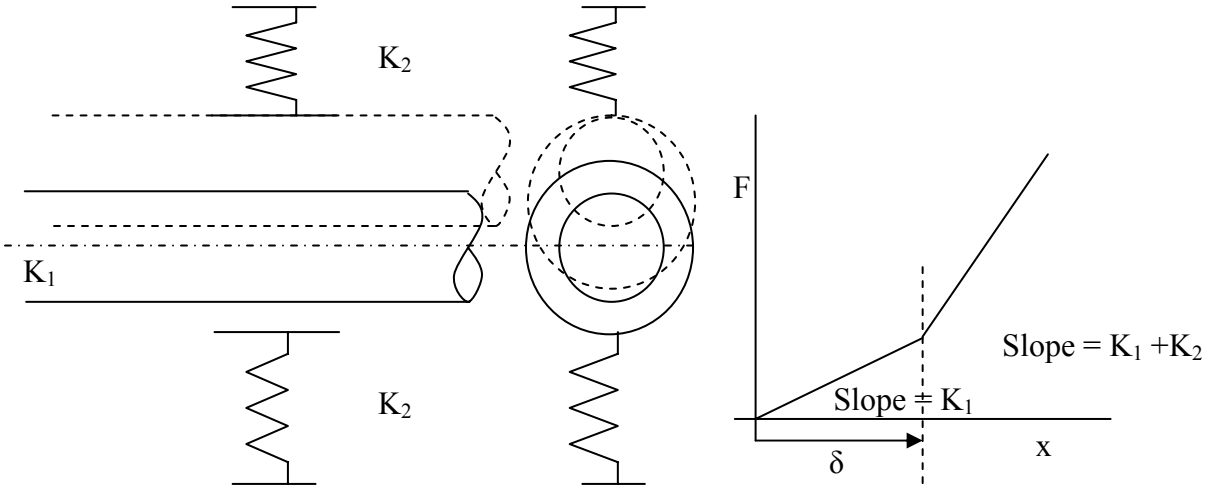

Fig 14: Rotor in intermittent contact with the stator

In Fig 14 the displacement of the stator is exaggerated as $K_2 >> K_1$.

Case A: Rotor at bearing center

Stiffness of the system = K_1

Undamped natural frequency = $\omega_1 = \sqrt{\frac{K_1}{m}}$

Case B: Rotor in constant contact with the stator

Equivalent stiffness of the system = $K_1 + K_2$

Undamped natural frequency = $\omega_2 = \sqrt{\frac{K_1 + K_2}{m}}$

Case C: Intermittent contact with the stator

The rotor "bounces" on the stator periodically leading to a piecewise linear stiffness of the system.

Equivalent stiffness of the system = $K_{eq} = K_1$ for $x < \delta$

$= K_1 + K_2$ for $x \geq \delta$

Natural Vibration Waveform from Intermittent Contact

Assuming that the rotor contacts just one side of the stator and the resultant vibration is not enough for it to contact the other side, the vibration waveform should be similar to Fig 15.

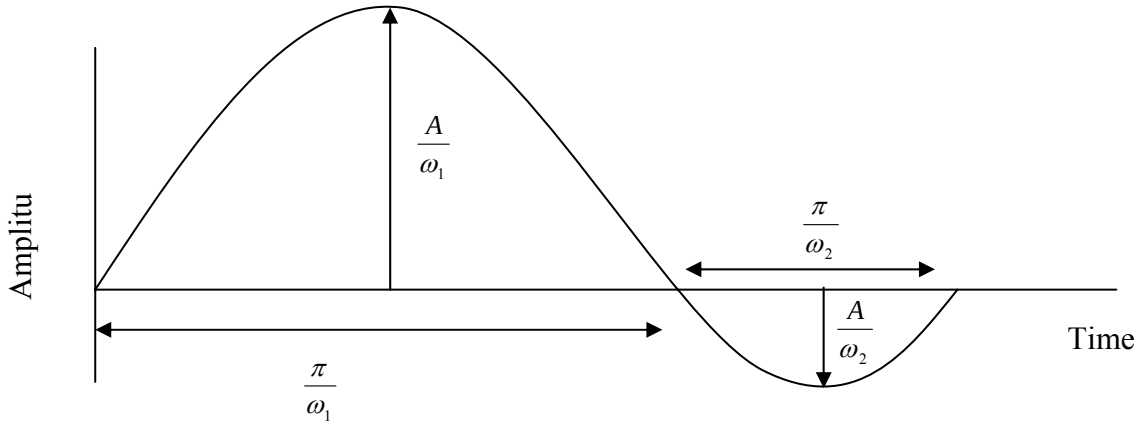

Fig 15: Natural vibration waveform of the rotor from intermittent contact

$$x(t) = A_1 \sin \omega_1 t \qquad \text{for} \quad 0 \le t < \frac{\pi}{\omega_1}$$

$$x(t) = -A_2 \sin\left[\omega_2 \{t - \frac{\pi}{\omega_1}\}\right] \quad \text{for} \quad \frac{\pi}{\omega_1} \le t < \frac{2\pi}{\omega} \qquad \text{(a)}$$

For the waveform to be differentiable at t = π/ω_1, x (t) has to be continuous and

$$\left.\frac{dx}{dt}\right|_{t \to \frac{\pi}{\omega_1}^+} = \left.\frac{dx}{dt}\right|_{t \to \frac{\pi}{\omega_1}^-}$$

or, $\omega_1 A_1 = \omega_2 A_2$

$A_1 = A/\omega_1$ and $A_2 = A/\omega_2$

The equivalent frequency is computed from the waveform:

$$\frac{2\pi}{\omega} = \frac{\pi}{\omega_1} + \frac{\pi}{\omega_2};$$
$$\omega = \frac{2\omega_1\omega_2}{\omega_1 + \omega_2} \qquad \text{(b)}$$

The Fourier coefficient C_n from the Fourier series expansion of equation (a) is given as:

$$C_n = \frac{A}{\pi\omega}\left[\frac{\left(\omega/\omega_2\right)^2}{1-n^2\left(\omega/\omega_2\right)^2} - \frac{\left(\omega/\omega_1\right)^2}{1-n^2\left(\omega/\omega_1\right)^2}\right] \times 2\cos\left(\frac{n\pi\omega}{2\omega_2}\right)$$

with a phase angle $\phi_n = \left(\frac{n\pi\omega}{2\omega_2}\right)$

The plot of the ratio of the second harmonic to the first harmonic amplitude indicates the presence of a large second harmonic component (Fig 16) in the excitation waveform for $\beta = 0.2$ (where $\beta = K_1/K_2$). A similar result is also obtained by the FFT of the waveform (Fig 15: Natural vibration waveform of the rotor from intermittent contact). It yields that the waveform has several higher harmonic components with only the second harmonic being comparable to the first in magnitude (Fig 17).

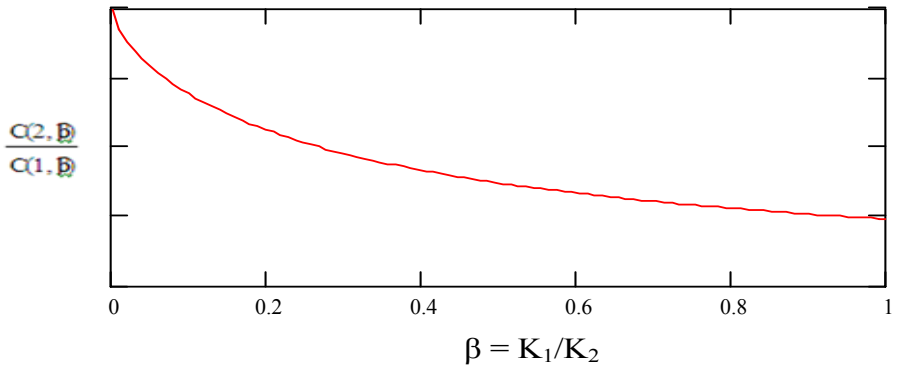

Fig 16: Plot of the ratio of the 1st and 2nd harmonic amplitude vs. β

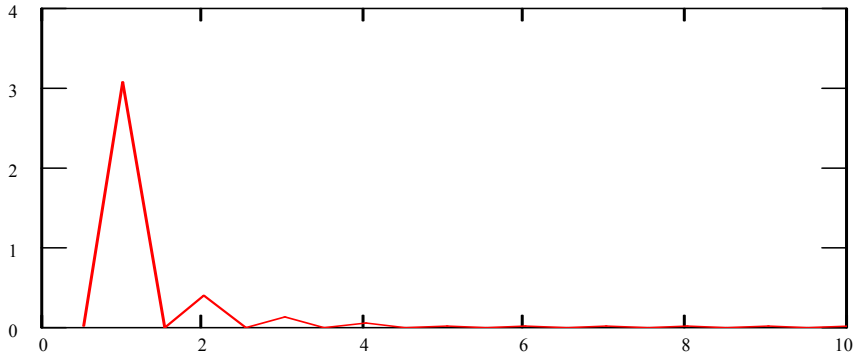

Fig 17: FFT of the vibration waveform

If the response of the non-linear system excited at 2ω (refer equation(b)) produces a subsynchronous vibration at a frequency of ω, then it can be concluded that it is vibration induced out of the inherent non-linearity in the system stiffness. The analog computer simulation results from the paper show likewise.

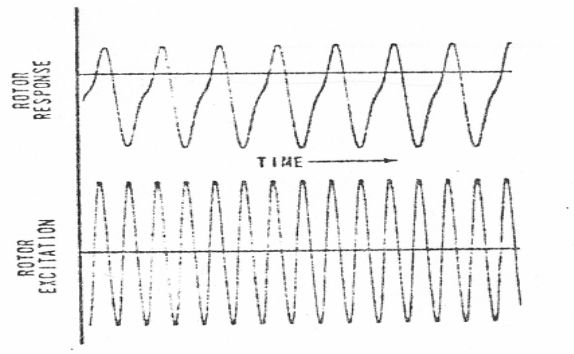

Fig 18: Analog computer simulation showing response to 2ω excitation for β=0.2

The analysis is now extended from considering a plane vibration case to a 'Short Rigid Rotor' model in the following chapter. Numerical methods will replace analog simulations.

CHAPTER IV

SHORT RIGID ROTOR MODEL TO SIMULATE INTERMITTENT CONTACT OF ROTOR WITH SINGLE STATOR SURFACE

Short Rigid Rotor Model

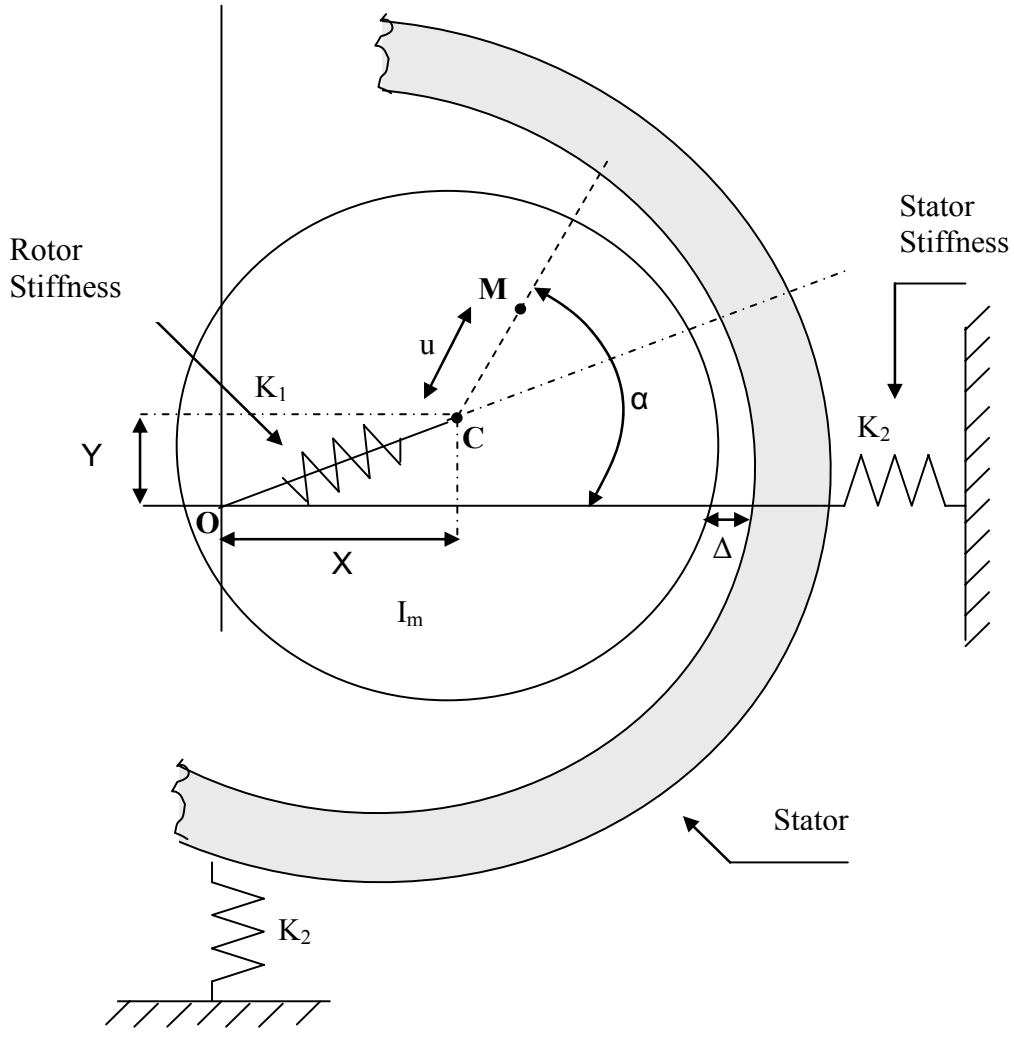

Fig 19: Rotordynamic model to analyze the effect of non-linear stiffness

The model illustrated in Fig 19 is used to simulate non-linear rotor-bearing stiffness due to intermittent contact of the rotor along the X-axis only. For simplicity, the bearing stiffness is assumed to be symmetric. The bearing stiffness is much greater than the rotor stiffness so that there is practically no displacement of the surface during contact. The frame of reference is fixed and the generalized coordinates are X, Y and α.

Equations of Motion

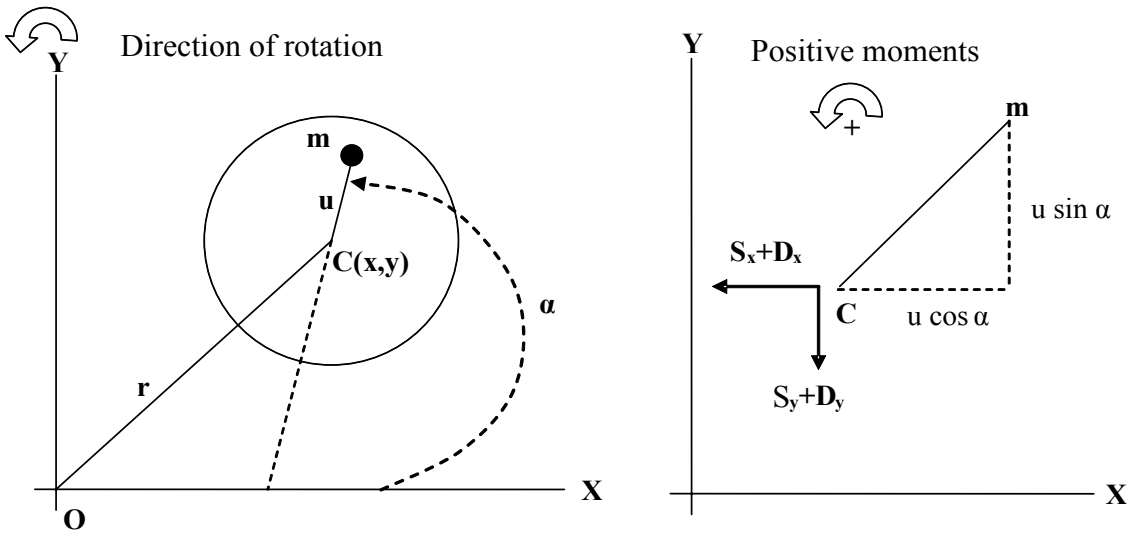

Fig 20: Free body diagram of the short rigid rotor

Generalized coordinate system: X, Y, α (Fig 20)

$$X_m = X + u\cos\alpha$$

$$Y_m = Y + u\sin\alpha$$

Differentiating with respect to time:

$$\dot{X}_m = \dot{X} - (u\sin\alpha)\dot{\alpha}$$

$$\dot{Y}_m = \dot{Y} + (u\cos\alpha)\dot{\alpha}$$

$$\ddot{X}_m = \ddot{X} - \{(u\sin\alpha)\ddot{\alpha} + \dot{\alpha}^2(u\cos\alpha)\}$$

$$\ddot{Y}_m = \ddot{Y} + \{(u\cos\alpha)\ddot{\alpha} - \dot{\alpha}^2(u\sin\alpha)\}$$

From Newton's Laws of Motion:

$$\sum F_x = m\ddot{X}$$

$$\sum F_y = m\ddot{Y}$$

$$\sum M = I_m\ddot{\alpha}$$

where,

F_x = restorative stiffness force (S_x) and 'damping force' (D_x) along the x-axis;

F_y = restorative stiffness force (S_y) and 'damping force' (D_y) along the y-axis;

M = moments taken about **m.**

$$m\ddot{X}_m = -K_x X - C\dot{X}$$

$$m\ddot{X}_m = m[\ddot{X} - \{(u\sin\alpha)\ddot{\alpha} + \dot{\alpha}^2(u\cos\alpha)\}] = -K_x X - C\dot{X}$$

$$m\ddot{X} + K_x X + C\dot{X} = mu\ddot{\alpha}\sin\alpha + m\dot{\alpha}^2 u\cos\alpha$$

Similarly,

$$m\ddot{Y} + K_y Y + C\dot{Y} = -mu\ddot{\alpha}\cos\alpha + m\dot{\alpha}^2 u\sin\alpha$$

Taking moments about **m**:-

$$I_m\ddot{\alpha} = K_y Y(u\cos\alpha) - K_x X(u\sin\alpha) - C\dot{X}(u\sin\alpha) + C\dot{Y}(u\cos\alpha)$$

$$I_m\ddot{\alpha} + K_x X(u\sin\alpha) + C\dot{X}(u\sin\alpha) - K_y Y(u\cos\alpha) - C\dot{Y}(u\cos\alpha) = 0$$

The equations of motion are:

$$m\ddot{X} + K_x X + C\dot{X} = mu\ddot{\alpha}\sin\alpha + m\dot{\alpha}^2 u\cos\alpha$$

$$m\ddot{Y} + K_y Y + C\dot{Y} = -mu\ddot{\alpha}\cos\alpha + m\dot{\alpha}^2 u\sin\alpha \qquad (1)$$

$$I_m\ddot{\alpha} + K_x X(u\sin\alpha) + C\dot{X}(u\sin\alpha) - K_y Y(u\cos\alpha) - C\dot{Y}(u\cos\alpha) = 0$$

For the particular case under consideration where the static stiffness of the rotor-bearing system changes as a step function of the rotor clearance (Δ) and hence the displacement along X, the system of equations (1) can be divided into two cases.

Case 1: $X < \Delta$

$K_x = K_y = K_1$

$$m\ddot{X} + K_1 X + C\dot{X} = mu\ddot{\alpha}\sin\alpha + m\dot{\alpha}^2 u\cos\alpha$$

$$m\ddot{Y} + K_1 Y + C\dot{Y} = -mu\ddot{\alpha}\cos\alpha + m\dot{\alpha}^2 u\sin\alpha \qquad (2)$$

$$I_m\ddot{\alpha} + K_1 X(u\sin\alpha) + C\dot{X}(u\sin\alpha) - K_1 Y(u\cos\alpha) - C\dot{Y}(u\cos\alpha) = 0$$

Case 2: $X \geq \Delta$

$K_x = K_1 + K_2$, $K_y = K_1$**

$$m\ddot{X} + (K_1 + K_2)X + C\dot{X} = mu\ddot{\alpha}\sin\alpha + m\dot{\alpha}^2 u\cos\alpha$$

$$m\ddot{Y} + K_1 Y + C\dot{Y} = -mu\ddot{\alpha}\cos\alpha + m\dot{\alpha}^2 u\sin\alpha \qquad (3)$$

$$I_m\ddot{\alpha} + (K_1 + K_2)X(u\sin\alpha) + C\dot{X}(u\sin\alpha) - K_1 Y(u\cos\alpha) - C\dot{Y}(u\cos\alpha) = 0$$

**Note that the stiffness changes only along the X-axis when contact occurs.

Non-Dimensional Equations of Motion

Case 1: X< Δ

$$m\ddot{X} + K_1 X + C\dot{X} = mu\ddot{\alpha}\sin\alpha + m\dot{\alpha}^2 u\cos\alpha$$

$$m\ddot{Y} + K_1 Y + C\dot{Y} = -mu\ddot{\alpha}\cos\alpha + m\dot{\alpha}^2 u\sin\alpha \quad (4)$$

$$\ddot{X} + \frac{K_1}{m}X + \frac{C}{m}\dot{X} = u\ddot{\alpha}\sin\alpha + \dot{\alpha}^2 u\cos\alpha$$

Let, $x = \frac{X}{u}$ and $\omega_1 = \sqrt{\frac{K_1}{m}}$

$$\ddot{x} + \omega_1^2 x + 2\xi\omega_1\dot{x} = \ddot{\alpha}\sin\alpha + \dot{\alpha}^2\cos\alpha$$

Let $\tau = \omega_1 t$;

$$\frac{dx}{dt} = \frac{dx}{d\tau}\times\frac{d\tau}{dt}; \frac{d\tau}{dt} = \omega_1$$

$$\frac{dx}{dt} = \omega_1\frac{dx}{d\tau}; \dot{x} = \omega_1\frac{dx}{d\tau}$$

$$\ddot{x} = \omega_1^2\frac{d^2x}{d\tau^2}$$

Similarly,

$$\dot{\alpha} = \omega_1\frac{d\alpha}{d\tau}; \ddot{\alpha} = \omega_1^2\frac{d^2\alpha}{d\tau^2}$$

Replacing in (4)

$$\ddot{x} + 2\xi\dot{x} + x = \dot{\alpha}^2 \cos\alpha + \ddot{\alpha}\sin\alpha$$

$$\ddot{y} + 2\xi\dot{y} + y = \dot{\alpha}^2 \sin\alpha - \ddot{\alpha}\cos\alpha$$

Moment equation:

$$I_m\ddot{\alpha} + K_1 X(u\sin\alpha) + C\dot{X}(u\sin\alpha) - K_1 Y(u\cos\alpha) - C\dot{Y}(u\cos\alpha) = 0 \qquad (5)$$

$Let, I_m = mG^2,$ where G = radius of gyration

$$Let, g = \frac{G}{u}$$

$$\therefore I_m = mu^2 g^2$$

Replacing in equation(5),

$$g^2\omega_1^2 \frac{d^2\alpha}{d\tau^2} + \omega_1^2 x\sin\alpha - \omega_1^2 y\cos\alpha + 2\xi\omega_1^2 \frac{dx}{d\tau}\sin\alpha - 2\xi\omega_1^2 \frac{dy}{d\tau}\cos\alpha = 0$$

$$or, \ddot{\alpha} + \frac{x}{g^2}\sin\alpha - \frac{y}{g^2}\cos\alpha + \frac{2\xi}{g^2}\dot{x}\sin\alpha - \frac{2\xi}{g^2}\dot{y}\cos\alpha = 0$$

Therefore, the non-dimensional set of equations for Case 1 is:

$$\ddot{x} + 2\xi\dot{x} + x = \dot{\alpha}^2 \cos\alpha + \ddot{\alpha}\sin\alpha$$

$$\ddot{y} + 2\xi\dot{y} + y = \dot{\alpha}^2 \sin\alpha - \ddot{\alpha}\cos\alpha \qquad (6)$$

$$\ddot{\alpha} + \frac{x}{g^2}\sin\alpha - \frac{y}{g^2}\cos\alpha + \frac{2\xi}{g^2}\dot{x}\sin\alpha - \frac{2\xi}{g^2}\dot{y}\cos\alpha = 0$$

Case 2: $X \geq \Delta$

$$m\ddot{X} + (K_1 + K_2)X + C\dot{X} = mu\ddot{\alpha}\sin\alpha + m\dot{\alpha}^2 u\cos\alpha$$

$$m\ddot{Y} + K_1 Y + C\dot{Y} = -mu\ddot{\alpha}\cos\alpha + m\dot{\alpha}^2 u\sin\alpha \quad (7)$$

$$\ddot{X} + \frac{(K_1 + K_2)}{m}X + \frac{C}{m}\dot{X} = u\ddot{\alpha}\sin\alpha + \dot{\alpha}^2 u\cos\alpha$$

Let, $x = \frac{X}{u}$, $\omega_1 = \sqrt{\frac{K_1}{m}}, \beta = \frac{K_1}{K_2}$

$$\omega_2 = \sqrt{\frac{(K_1 + K_2)}{m}} = \sqrt{\frac{K_1}{m} \times \frac{(K_1 + K_2)}{K_1}} = \omega_1\sqrt{1 + \frac{1}{\beta}}$$

$$or, \ddot{x} + \omega_2^2 x + 2\xi\omega_1\dot{x} = \ddot{\alpha}\sin\alpha + \dot{\alpha}^2\cos\alpha$$

$$or, \ddot{x} + \omega_1^2\left(1 + \frac{1}{\beta}\right)x + 2\xi\omega_1\dot{x} = \ddot{\alpha}\sin\alpha + \dot{\alpha}^2\cos\alpha$$

Let $\tau = \omega_1 t$;

Non dimensional forms of equation (7) are:

$$\ddot{x} + 2\xi\dot{x} + x\left(1 + \frac{1}{\beta}\right) = \dot{\alpha}^2\cos\alpha + \ddot{\alpha}\sin\alpha$$

$$\ddot{y} + 2\xi\dot{y} + y = \dot{\alpha}^2\sin\alpha - \ddot{\alpha}\cos\alpha$$

Moment equation:

$$I_m\ddot{\alpha}+\left(K_1+K_2\right)X(u\sin\alpha)+C\dot{X}(u\sin\alpha)-K_1Y(u\cos\alpha)-C\dot{Y}(u\cos\alpha)=0$$

$$\Rightarrow I_m\ddot{\alpha}+K_1\left(1+\frac{1}{\beta}\right)X(u\sin\alpha)+C\dot{X}(u\sin\alpha)-K_1Y(u\cos\alpha)-C\dot{Y}(u\cos\alpha)=0 \tag{8}$$

Non-dimensional form of equation (8) is:

$$\ddot{\alpha}+\frac{x}{g^2}\left(1+\frac{1}{\beta}\right)\sin\alpha-\frac{y}{g^2}\cos\alpha+\frac{2\xi}{g^2}\dot{x}\sin\alpha-\frac{2\xi}{g^2}\dot{y}\cos\alpha=0$$

Therefore, the non-dimensional set of equations for Case 2 is:

$$\ddot{x}+2\xi\dot{x}+x\left(1+\frac{1}{\beta}\right)=\dot{\alpha}^2\cos\alpha+\ddot{\alpha}\sin\alpha$$

$$\ddot{y}+2\xi\dot{y}+y=\dot{\alpha}^2\sin\alpha-\ddot{\alpha}\cos\alpha \tag{9}$$

$$\ddot{\alpha}+\frac{x}{g^2}\left(1+\frac{1}{\beta}\right)\sin\alpha-\frac{y}{g^2}\cos\alpha+\frac{2\xi}{g^2}\dot{x}\sin\alpha-\frac{2\xi}{g^2}\dot{y}\cos\alpha=0$$

Euler Integration Scheme

Equations (6) and (9) are integrated using Euler's method to obtain the response of the system modeled for unbalance excitation. The following substitutions are made:

$$x=u_1;\dot{x}=u_2;y=u_3;\dot{y}=u_4;\alpha=u_5;\dot{\alpha}=u_6$$

Case 1: For $x < \delta$ (where $\delta = \frac{\Delta}{u}$)

$$\dot{u}_2 = -2\xi u_2 - u_1 + u_6{}^2 \cos u_5 + \dot{u}_6 \sin u_5$$

$$\dot{u}_4 = -2\xi u_4 - u_3 + u_6{}^2 \sin u_5 - \dot{u}_6 \cos u_5 \tag{10}$$

$$\dot{u}_6 = -\frac{u_1}{g^2} \sin u_5 + \frac{u_3}{g^2} \cos u_5 - \frac{2\xi}{g^2} u_2 \sin u_5 + \frac{2\xi}{g^2} u_4 \cos u_5$$

Case 2: For $x \geq \delta$

$$\dot{u}_2 = -2\xi u_2 - u_1 \left(1 + \frac{1}{\beta}\right) + u_6{}^2 \cos u_5 + \dot{u}_6 \sin u_5$$

$$\dot{u}_4 = -2\xi u_4 - u_3 + u_6{}^2 \sin u_5 - \dot{u}_6 \cos u_5 \tag{11}$$

$$\dot{u}_6 = -\frac{u_1}{g^2}\left(1 + \frac{1}{\beta}\right) \sin u_5 + \frac{u_3}{g^2} \cos u_5 - \frac{2\xi}{g^2} u_2 \sin u_5 + \frac{2\xi}{g^2} u_4 \cos u_5$$

Time - marching scheme

$$u_1(t + \delta t) = u_1(t) + u_2(t)\delta t$$

$$u_2(t + \delta t) = u_2(t) + \dot{u}_2(t)\delta t$$

$$u_3(t + \delta t) = u_3(t) + u_4(t)\delta t$$

$$u_4(t + \delta t) = u_4(t) + \dot{u}_4(t)\delta t$$

$$u_5(t + \delta t) = u_5(t) + u_6(t)\delta t$$

$$u_6(t + \delta t) = u_6(t) + \dot{u}_6(t)\delta t$$

Numerical Simulation

Numerical integration of equations (10) and (11) with different initial conditions is used to simulate an experimental rotor rig with non-linear bearing stiffness. The system parameters are set to closely represent the actual rotor. The numerical model is excited by unbalance. Details of the experimental set up have been provided in the next chapter.

The stiffness ratio $K_1/K_2 = \beta$ for the rotor bearing system is 0.23. It is necessary to find out the non-dimensional critical frequency of the waveform described by Ehrich.

$$\omega = \frac{2\omega_1\omega_2}{\omega_1 + \omega_2}$$

$$\frac{\omega_2}{\omega_1} = \sqrt{\frac{K_1 + K_2}{K_1}} = \sqrt{1 + \frac{1}{\beta}}$$

$$\omega = \frac{2\omega_1\sqrt{1 + \frac{1}{\beta}}}{1 + \sqrt{1 + \frac{1}{\beta}}}$$

The non-dimensional response waveform for the rotor rotating at the critical speed can be represented as:

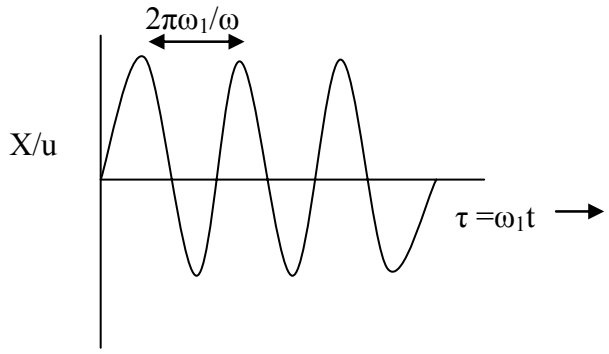

Fig 21: Non-dimensional waveform at the critical speed

The frequency of the waveform (Fig 21) is:

$f = \frac{1}{T} = \frac{\omega}{2\pi\omega_1}$, where ω is the running speed.

For a linear system (large clearance) $\omega = \omega_1$,

$f = \frac{1}{2\pi} = 0.16$ *

The first non-dimensional critical frequency is given as:

$$f = \frac{2\omega_1\sqrt{1+\frac{1}{\beta}}}{2\pi\omega_1(1+\sqrt{1+\frac{1}{\beta}})} = \frac{\sqrt{1+\frac{1}{\beta}}}{\pi(1+\sqrt{1+\frac{1}{\beta}})} \qquad (12)$$

For the experimental rotor, β = 0.23,

$f = 0.222$

*This value provides a check to see if the numerical integration has been correctly executed.

Simulation of large rotor-stator clearance with no contact - model verification

A likely proof of the verity of the numerical model will be to obtain the response of the system to a large clearance (no contact) for different rotational speeds. The maximum response to unbalance should occur at $f = \frac{1}{2\pi} = 0.16$. The initial conditions of the rotor are shown below (Fig 22). Note that 'alphadot' is the rotating speed.

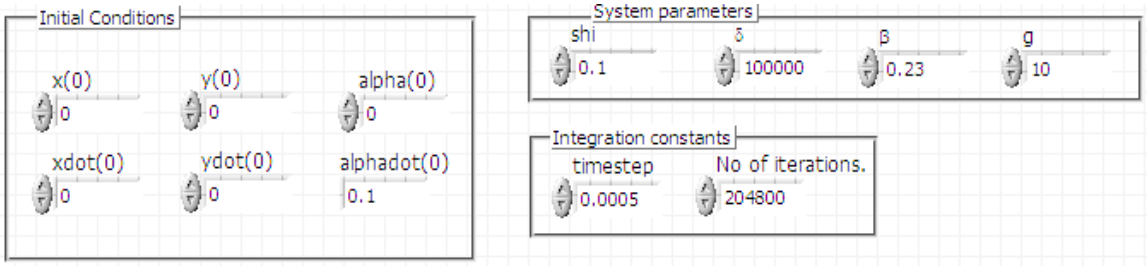

Fig 22: Initial values and system settings. A large value of δ ensures a linear system.

Integration with increasing values of 'alphadot (0)' or the rotating speed shows a large synchronous response at $f = 0.16$ (Fig 23) as predicted by theory.

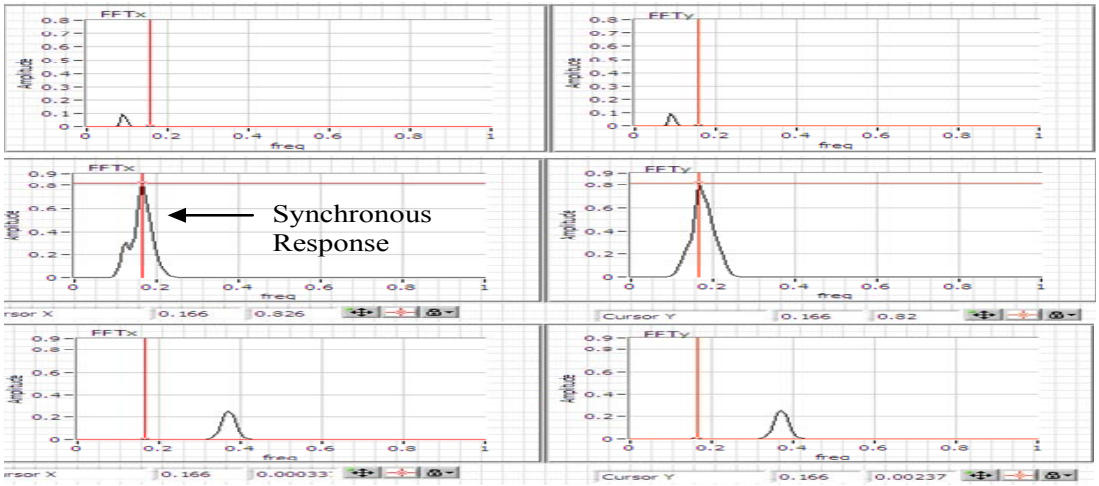

Fig 23: Synchronous response for no contact

Simulation of small clearance with contact

The clearance is reduced to δ = 0.2 (Fig 24) and simulations re-run.

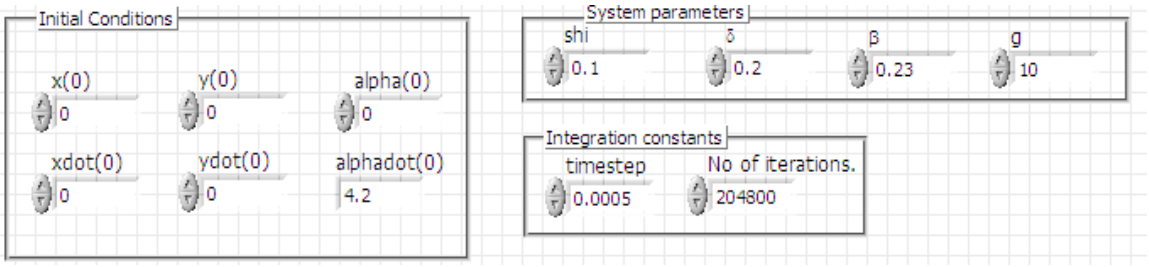

Fig 24: Initial and parametric constants to simulate small rotor-stator clearance. δ = 0.2

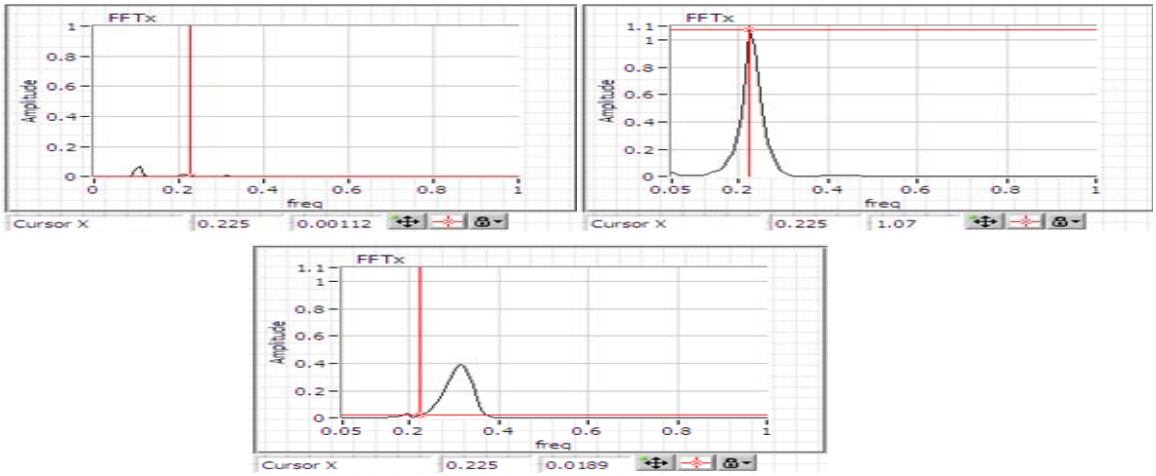

Fig 25: Response with small clearance at different rotational speeds

With a non-linear stiffness along the x-axis, the non-dimensional critical frequency is 0.225 (Fig 25). At a speed lower than the critical frequency, the spectrum of X shows higher harmonic components (Fig 26). Y has a clean spectrum.

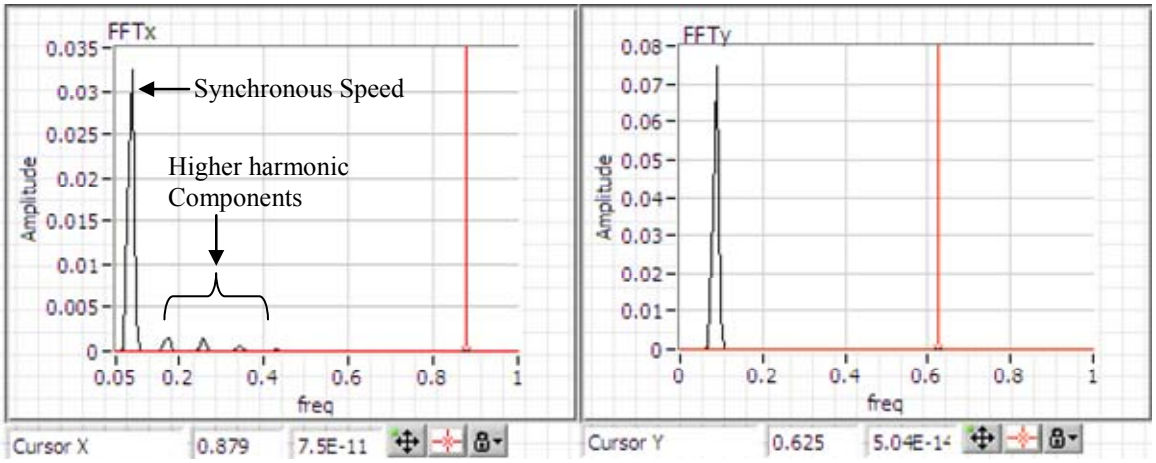

Fig 26: Higher harmonics on the X –spectrum at a speed lower than the critical

The time waveform (Fig 27) also illustrates that collision occurs along the X – axis clipping the wave.

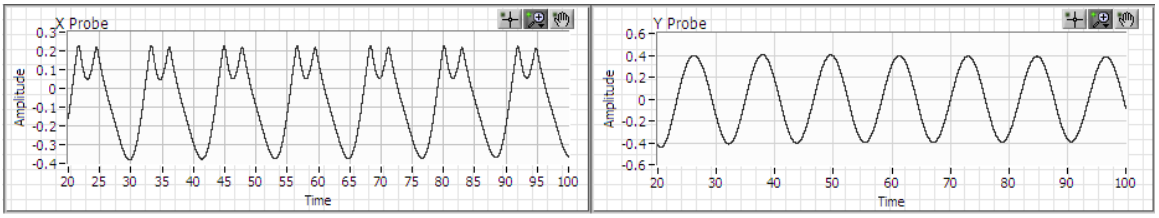

Fig 27: Time waveform at a speed lower than the critical

"Frequency demultiplication" – Large subsynchronous response at twice the critical speed

When the rotor speed is twice the critical speed, a large subsynchronous component (Fig 28) on the X-spectrum at exactly the critical frequency is noted. The Y-response is largely synchronous. The orbit shows the proverbial inside loop.

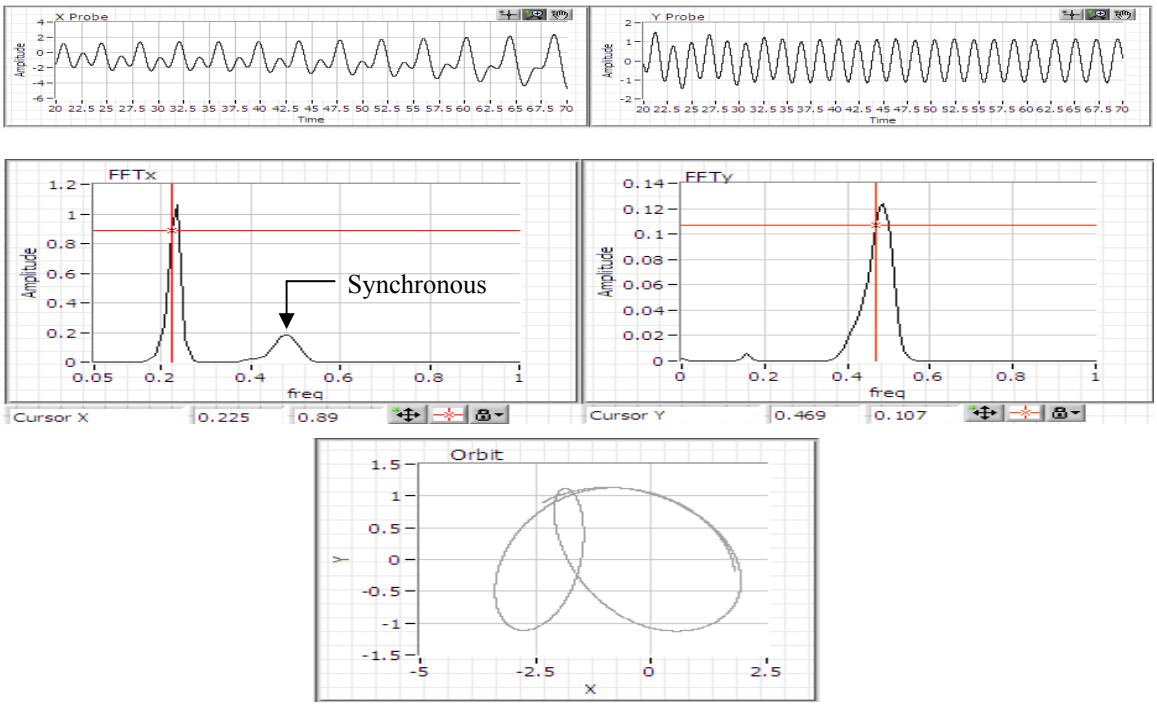

Fig 28: Vibration signatures at twice the critical speed – time trace, spectra and orbit

On increasing the speed, the subsynchronous vibration disappears indicating that the rotor-bearing system is not unstable (Fig 29).

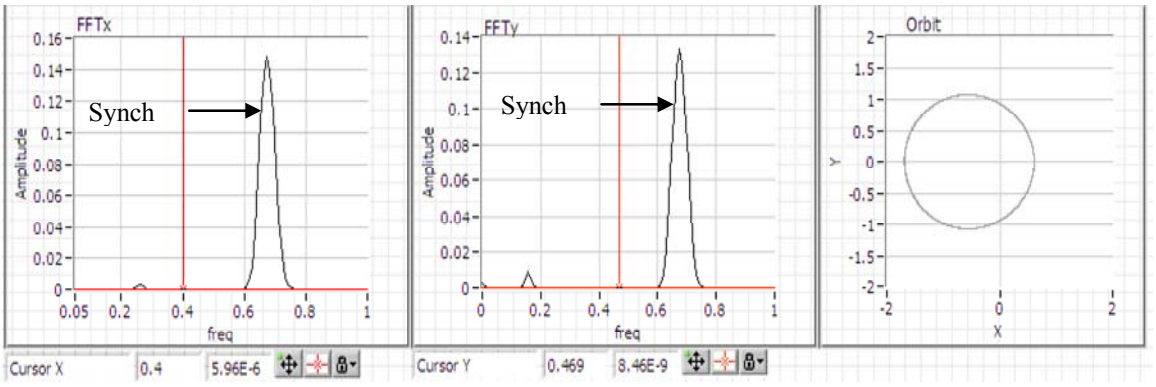

Fig 29: Subsynchronous vibration disappears on increasing the speed

CHAPTER V

EXPERIMENTAL DETERMINATION OF ROTOR BEHAVIOR INDUCED FROM NON-LINEAR ROTOR-BEARING STIFFNESS

Numerical simulations from the rotordynamic model in the previous chapter have yielded typical response to non-linear stiffness which might be used as diagnostic tools in rotating machinery monitoring. Of particular interest is the peculiar subsynchronous vibration phenomenon which occurs at twice the critical speed. This chapter shows the occurrence of "frequency demultiplication" experimentally. A rotor rig was set up to produce non-linear bearing support stiffness and the signals generated from orthogonally mounted proximity probes were studied in detail.

Experimental Setup – Rig Description and Instrumentation

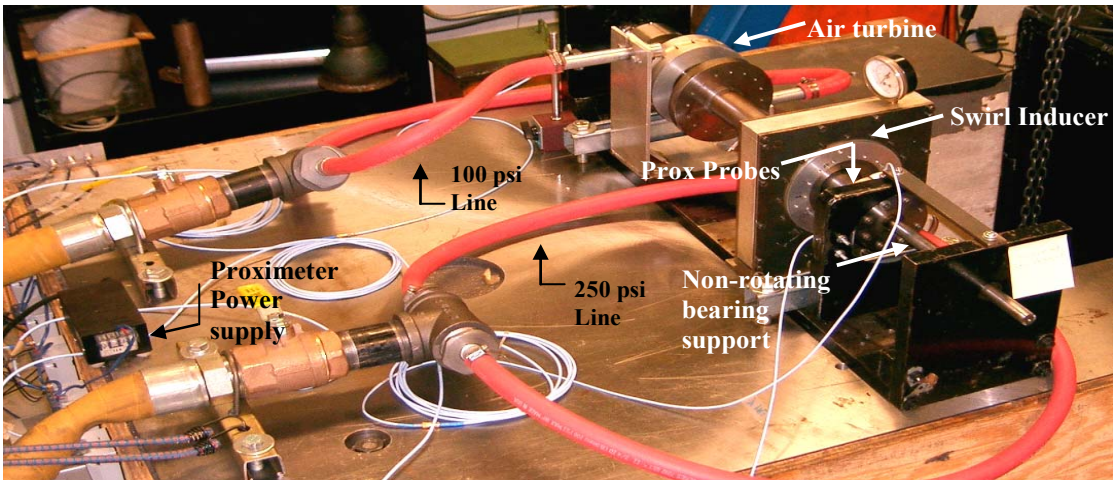

Fig 30: Experimental rig

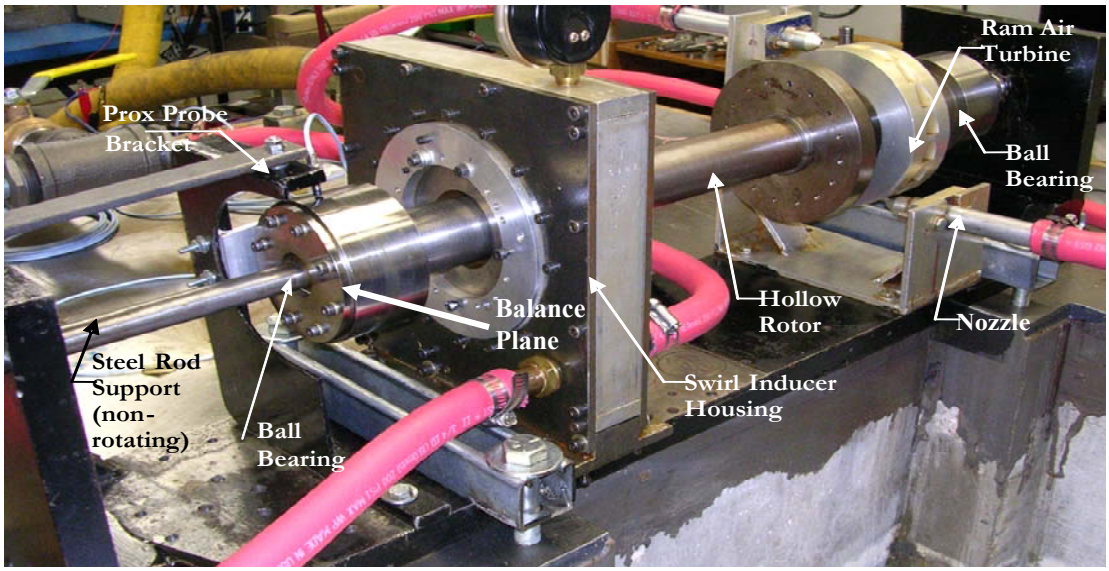

Fig 31: Closer view of the rig

The rotor (Fig 30 and Fig 31) is mounted on ball bearings constrained at the inner race by a non-rotating cantilevered steel support rod. Pressurized air drives the air-turbine upto a maximum speed of 6000 rpm. The swirl inducer housing has nozzles arranged around the periphery of the rotor to induce air swirl when pressurized. The air swirl is in the direction of rotor rotation and generates whirl instability from destabilizing cross coupled stiffness above the first critical speed (2100 rpm). A sectional view of the swirl inducer chamber is shown in Fig 32.

Two calibrated orthogonally mounted eddy current proximity probes were used to capture vibration data from the rotor. Another proximity probe was used to read tachometer pulses from a raised notch on the rotor surface. LVTRC was used for all data acquisition and analysis. The rotor was modeled using XLTRC^2 (Appendix II) after the stiffness of the bearings at the inducer end and the air turbine end were measured in

horizontal and vertical directions. The values were used as bearing inputs and minimal damping was assumed. The first mode shape (Fig 33) of the rotor showed that the balance plane should be as close to the inducer end bearing as possible. Fig 31 shows the balance plane. The single plane orbit method was used to balance the rotor to acceptable limits of vibration.

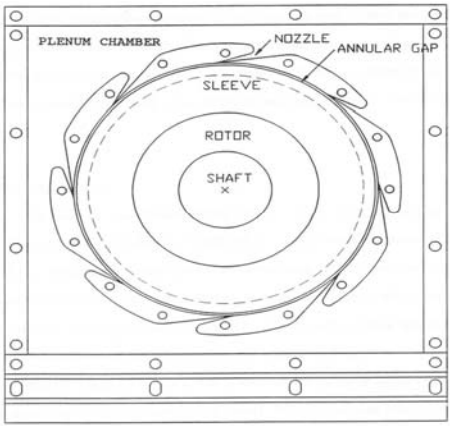

Fig 32: Swirl inducer sectional view

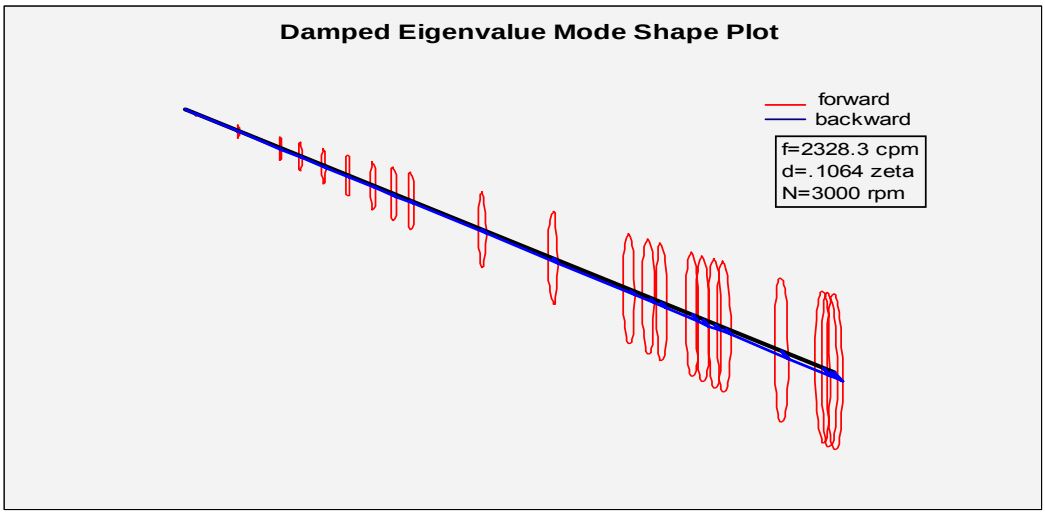

Fig 33: First forward mode shape

Introducing Non-linear Bearing Stiffness in the Rig

In order to introduce non-linearity in the bearing stiffness as a step function of the displacement along the horizontal axis, a stiffener was constructed and mounted as shown in Fig 34.

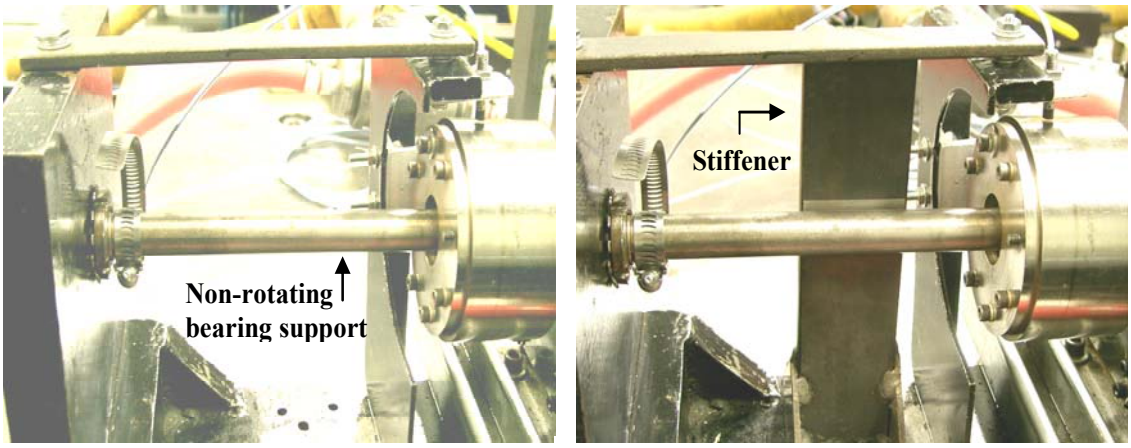

Fig 34: Non-rotating bearing support without and with stiffener

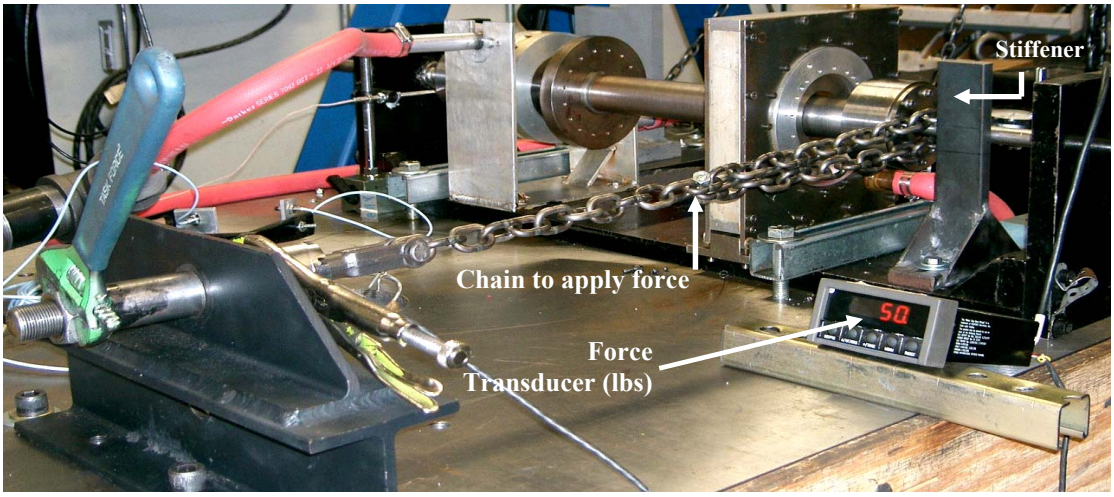

Fig 35: Stiffness measurements at the bearing

A force transducer and a dial gauge was used (Fig 35 and Fig 36) to estimate the stiffness at the bearing location and ensure that the force against displacement plot (Fig 37) showed the same step function characteristic as in Ehrich's 1966 paper.

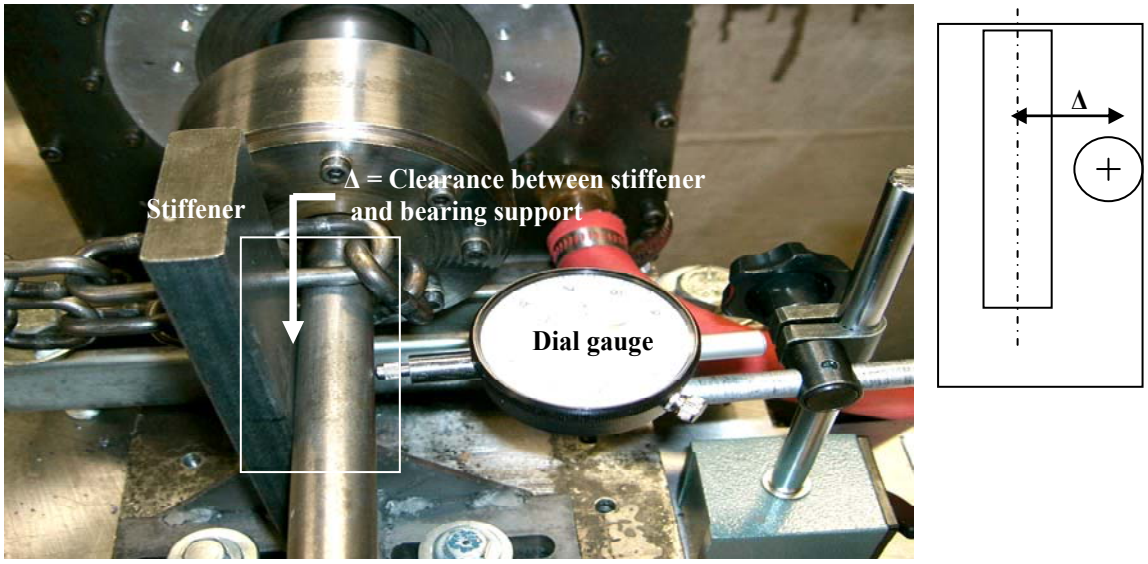

Fig 36: Close-up view of the stiffener

F in lb	X in inches
0	0.00
5	0.00050
11	0.00110
15	0.00150
21	0.00210
26	0.00260
31	0.00310
41	0.00410
50	0.00500
70	0.00700
90	0.00900
100	0.01000

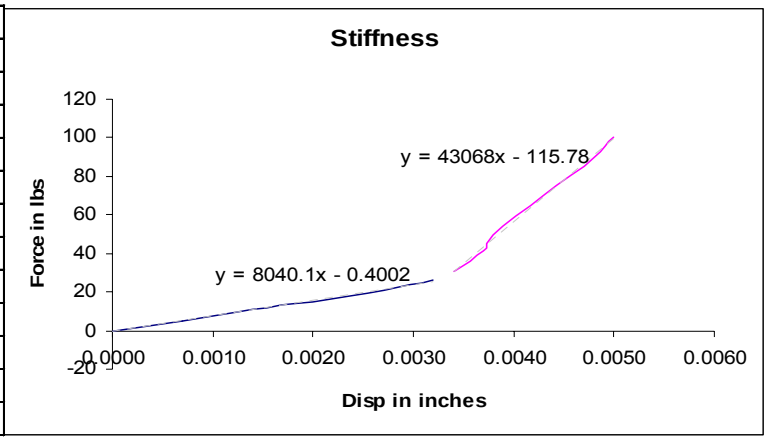

Fig 37: Non-linear stiffness of the bearing

Experimental Results with Non-linear Bearing Stiffness

Initial experiments were performed with the stiffener mounted at varying clearances from the non-rotating bearing support till satisfactory results were obtained. Fig 37 is such a case and all results reported below (unless otherwise mentioned) pertain to that case.

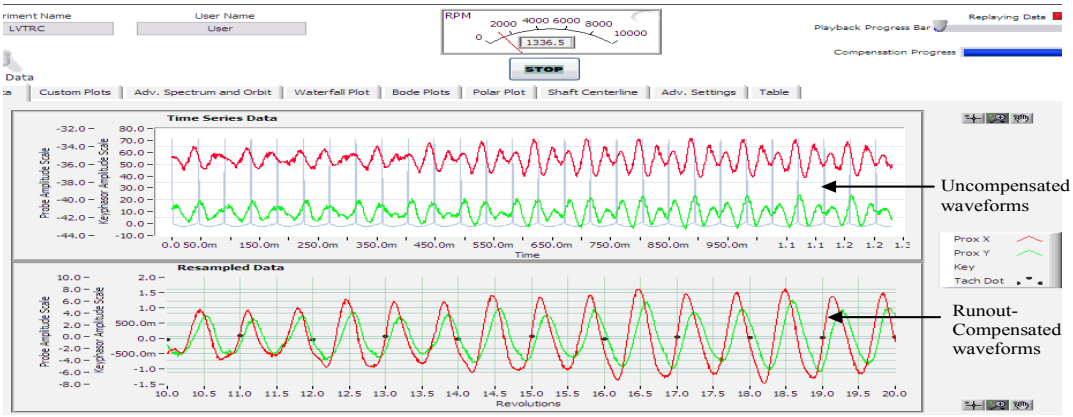

Fig 38: X and Y probe signals at 1300 RPM - below the critical speed

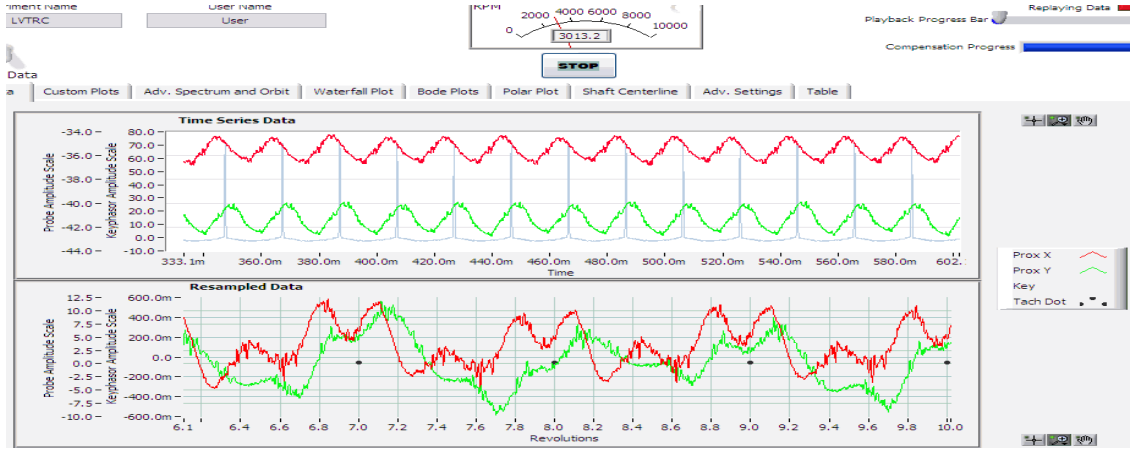

Fig 39: Probe signals at 3000 RPM – above the first critical

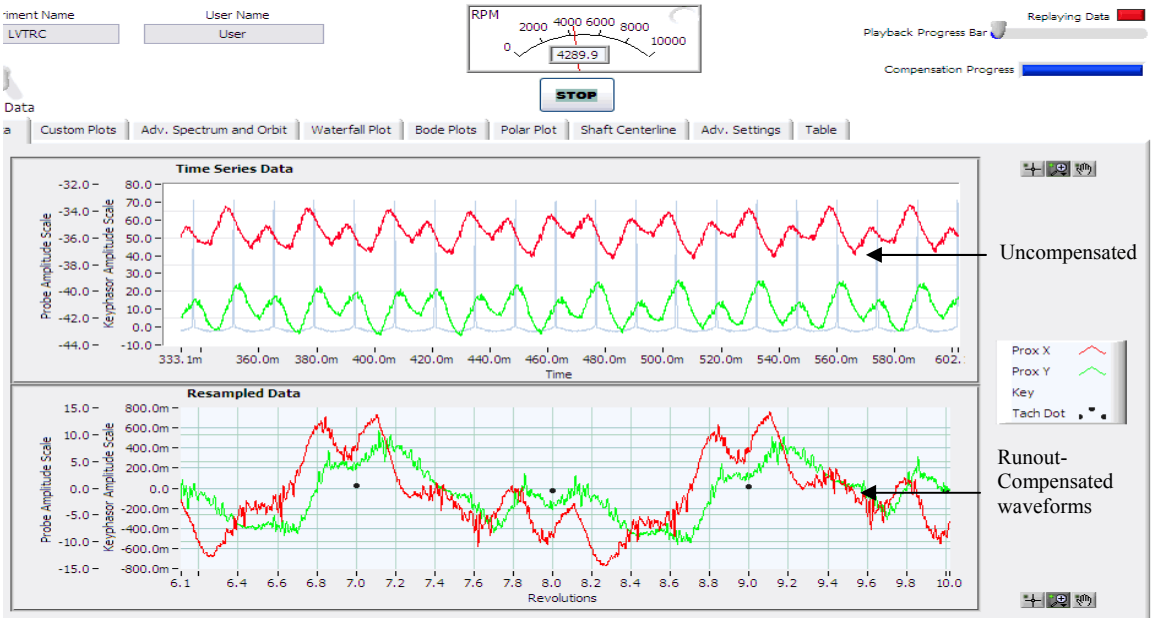

Fig 40: Frequency demultiplication at twice the critical speed

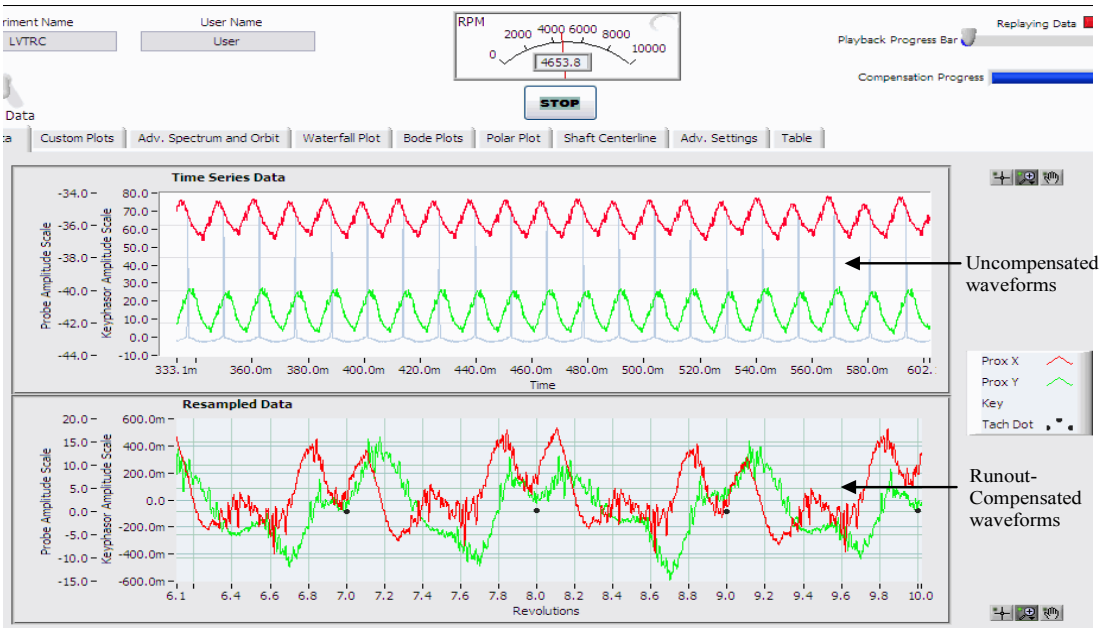

Fig 41: Probe signals at 4600 RPM

Fig 38 - Fig 41 demonstrate how the rotor behavior changes as the effect of non-linear stiffness sets in with increasing speed. At low speeds (below the critical, Fig 38) the runout-compensated waveforms resemble sinusoids, indicating that the vibration is mainly 1X from unbalance excitation. At higher speeds (above the first critical, Fig 39) the X-probe signal is clipped (the stiffener is mounted along the X-axis) and also shows the presence of higher harmonic components. Fig 40 illustrates the phenomenon of frequency demultiplication as analyzed by Ehrich [5] with his planar model. Note that the compensated probe signals at twice the critical speed (2 x 2010 RPM) shown on the 'Resampled' plot take two revolutions (x-axis scale shows the number of revolutions) to complete one cycle. The phenomenon disappears as the rotor speed increases (Fig 41) and the waveforms return to one cycle per revolution.

Frequency spectrum at various speeds

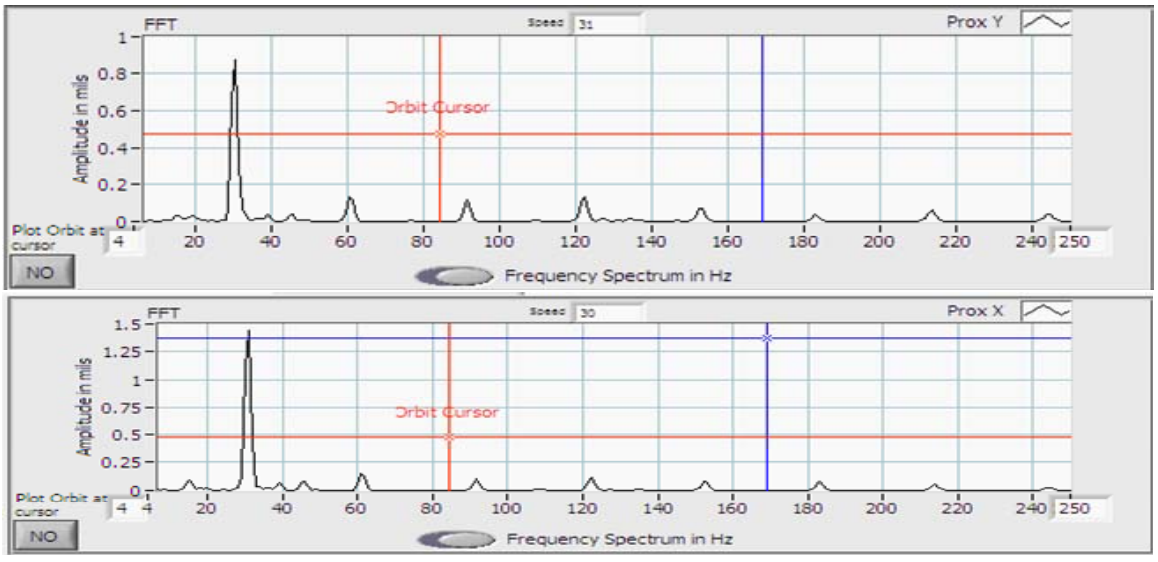

Fig 42: Spectrum at 1800 RPM indicate the presence of higher harmonics

Fig 42 shows the presence of higher harmonics in the frequency spectrum below the critical speed and is consonant with the numerical simulation results.

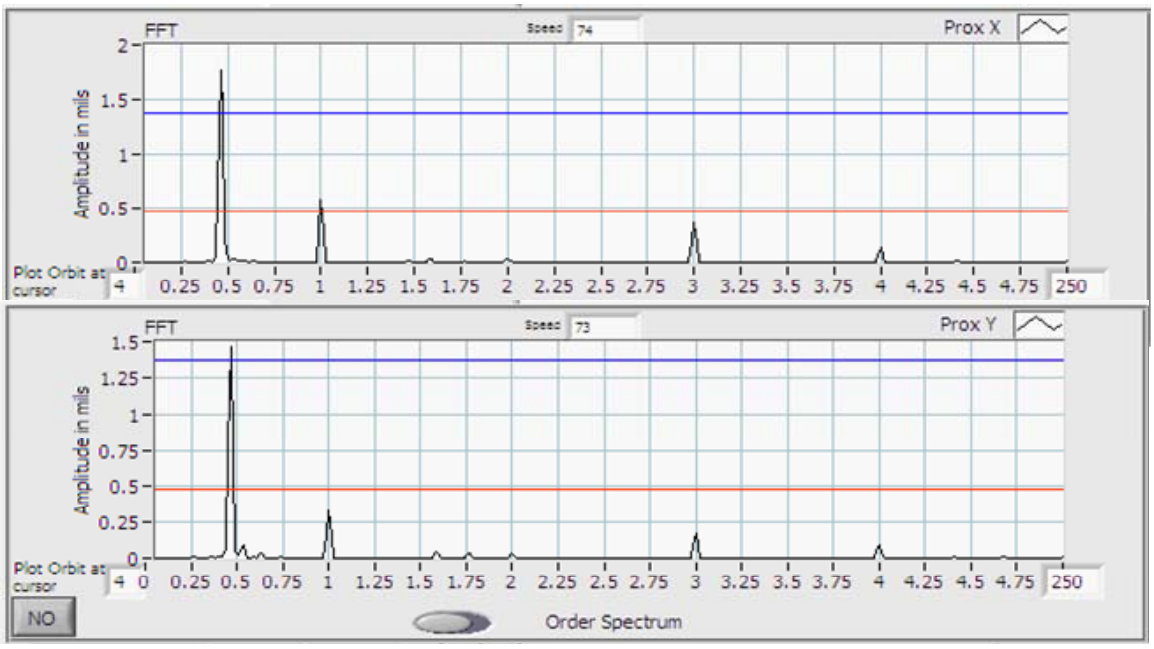

Fig 43: Subsynchronous vibration at 4200 RPM at 0.5X

The order spectrum at 4200 RPM (Fig 43) indicates the presence of a large subsynchronous vibration which can be easily mistaken for instability. However as proved in numerical and empirical results above, non-linear stiffness at the bearings causes the large subsynchronous vibration at twice the first critical speed. A useful diagnostic feature of such a case is that the subsynchronous component disappears quickly when the speed is increased slightly as shown in Fig 44 .

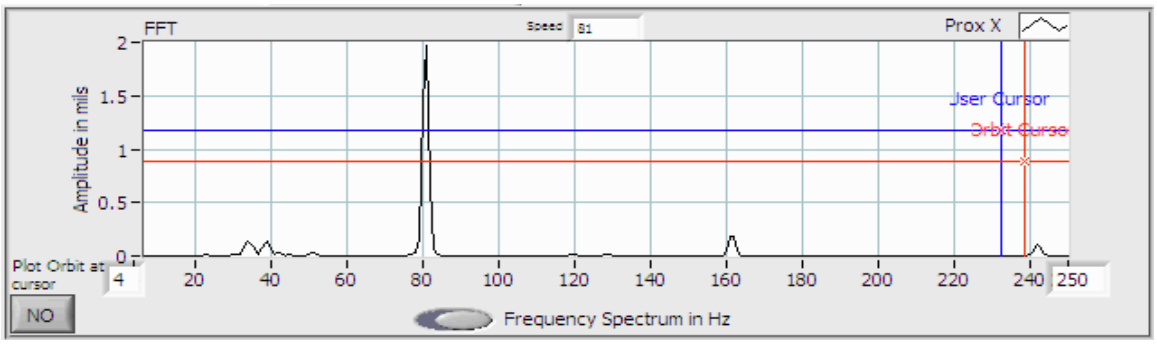

Fig 44: Subsynchronous vibration disappears on increasing the speed

A waterfall plot (Fig 45) summarizes the conclusions above.

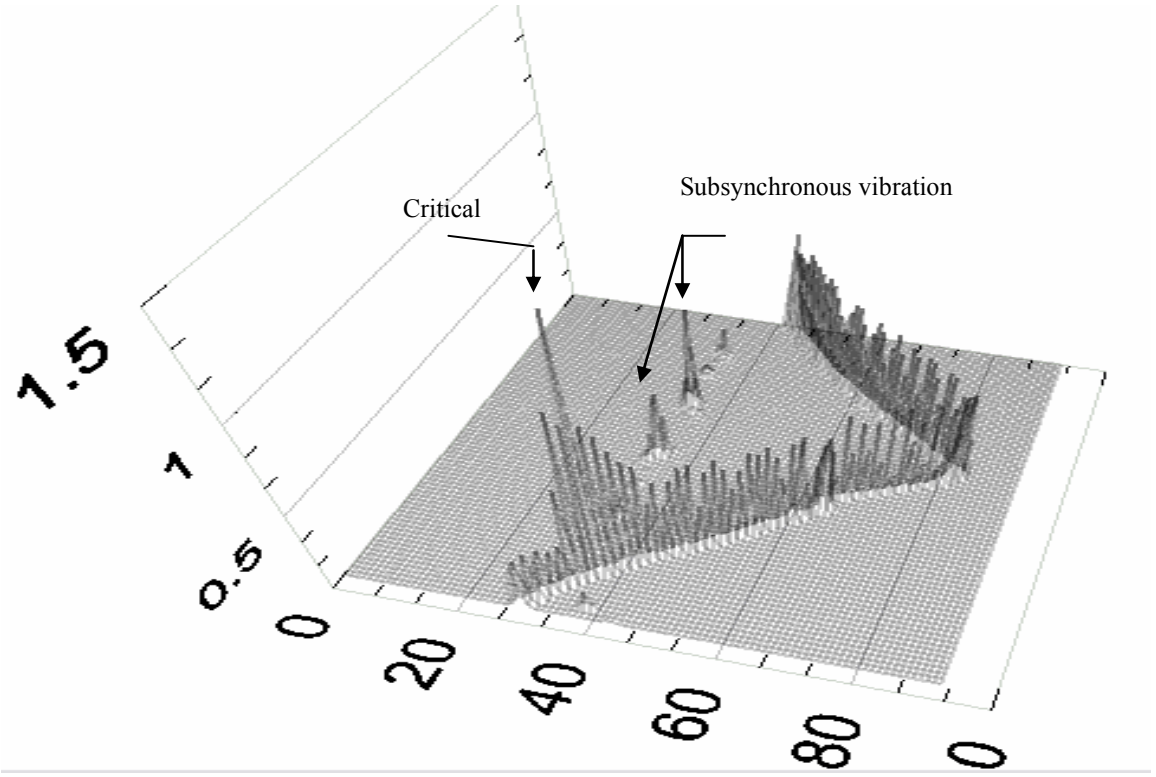

Fig 45: Waterfall plot from the X-probe showing the onset of subsynchronous vibration at 0.5X

Orbit Plots

The orbit plots (Fig 46) exhibit an inside loop at twice the critical speed but is transitory. With a slight change in speed, the loop disappears. The orbits bear similarities with those predicted from the numerical simulations.

Fig 46: Orbits before, at and after the onset of subsynchronous vibration at twice the critical speed
From an analog oscilloscope

Experimental Results – Linear System

The results from the previous section are compared to the case where the rotor-bearing stiffness was linear throughout its operating speed range. Measurements were made with the nonlinear stiffener removed. The frequency spectrum does not show any significant higher harmonic components, nor is there any large subsynchronous component of vibration (Fig 47).

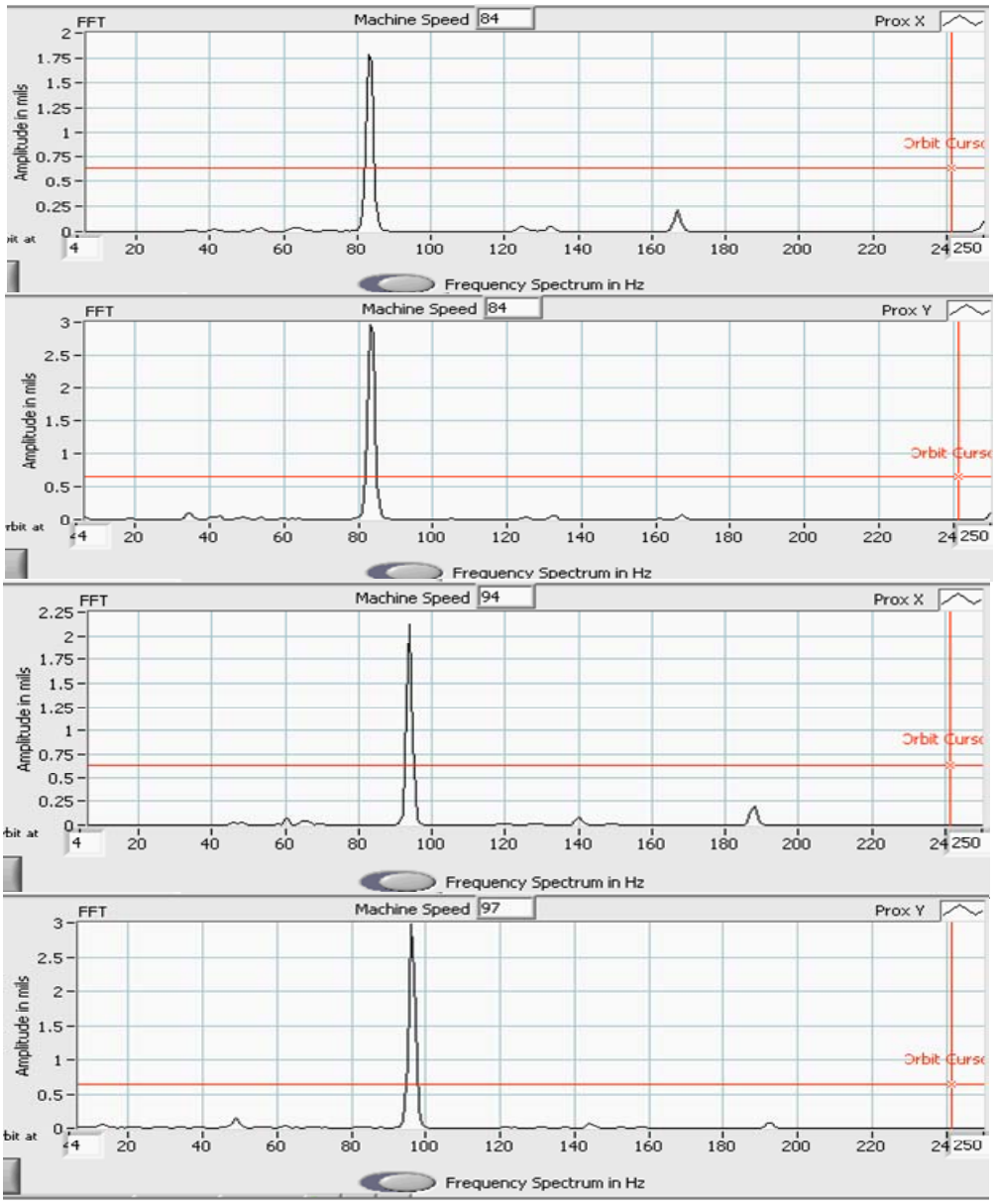

Fig 47: Frequency spectrum for linear bearing support at different running speeds

It can be concluded from the above experiments and analysis that non-linearity in stiffness of a rotor-bearing system induces a large subsynchronous vibration when rotating at twice the critical speed. The vibration disappears on increasing the speed.

CHAPTER VI

DIAGNOSING UNSTABLE SUBSYNCHRONOUS VIBRATIONS USING THE SYNCHRONOUS PHASE ANGLE

Instability and Cross-coupled Stiffness

Mathematically, dynamic instability is defined as a solution to the linear differential equations of motion characterized by a complex eigenvalue with a positive real part. The vibration amplitude associated with instability becomes unbounded (infinitely large), if linear stability theory holds. In practice, the vibration with growing amplitude will cause seals or blades to rub or it will reach a 'limit cycle' due to non-linearities in the system e.g. damping increases with amplitude. In rotordynamics, negative direct damping seldom occurs. Instead cross coupled stiffness, modeled as a follower force driving the forward going whirl orbit is usually the factor responsible for instability.

The Jeffcott rotor model with cross coupled stiffness is a modal model for any real machine operating through its first critical speed. It may be represented mathematically as:

$$\begin{aligned} m\ddot{x} + c\dot{x} + kx + k_{xy}y &= m\omega^2 u\cos\omega t \\ m\ddot{y} + c\dot{y} + ky + k_{yx}x &= m\omega^2 u\sin\omega t \end{aligned} \qquad (13)$$

It is found that for the particular case where $k_{xy} = -k_{yx} = \mathcal{K}$; $\mathcal{K} > \mathbf{0}$; the cross coupled forces drive the rotor unstable in forward whirl (the common mode in real machines). It

represents a type of force induced by fluid forces around a turbine, impeller, or fluid seal, or internal friction.

The particular solution to equation (13) is of interest. The amplitude and phase of synchronous vibration is given as:

$$| r |=| \sqrt{x^2 + y^2} |= \frac{m\omega^2 u}{\sqrt{(k - m\omega^2)^2 + (\omega c - \mathcal{K})^2}}$$

$$\beta = \tan^{-1}\left[\frac{\omega c - \mathcal{K}}{k - m\omega^2}\right] \tag{14}$$

In effect, the equivalent damping due to cross coupled stiffness becomes,

$$c_e = c - \frac{\mathcal{K}}{\omega}, \tag{15}$$

which is a function of the magnitude of cross coupled stiffness and the speed of rotation. Noticeably, the synchronous phase angle β is also affected by the cross coupled stiffness. It therefore can be a useful diagnostic value to determine whether the rotating system can have negative equivalent damping (instability)! As shown by equation (14), both backward ($\mathcal{K} < 0$) and forward ($\mathcal{K} > 0$) cross coupled follower forces will change the damping and the value of β - the former increasing and the latter reducing it. However, backward driving cross-coupled stiffness is rare, a soft continuous rotor rub being one of the few examples. It is the case of forward driving cross coupling that is the cause of most instabilities and the need arises to find how 'β' changes in this case. A plot of β against rotating speed for various values of $\mathcal{K}$ is educative (Fig 48).

$$shi := 0.1 \qquad wn := 60 \qquad K := 90000 \qquad w := 0..120$$

$$beta(w,k) := \left[\frac{180}{\pi}\cdot atan\left[\frac{\left(2\cdot shi\cdot\frac{w}{wn}-\frac{k}{K}\right)}{1-\left(\frac{w}{wn}\right)^2}\right]\right]$$

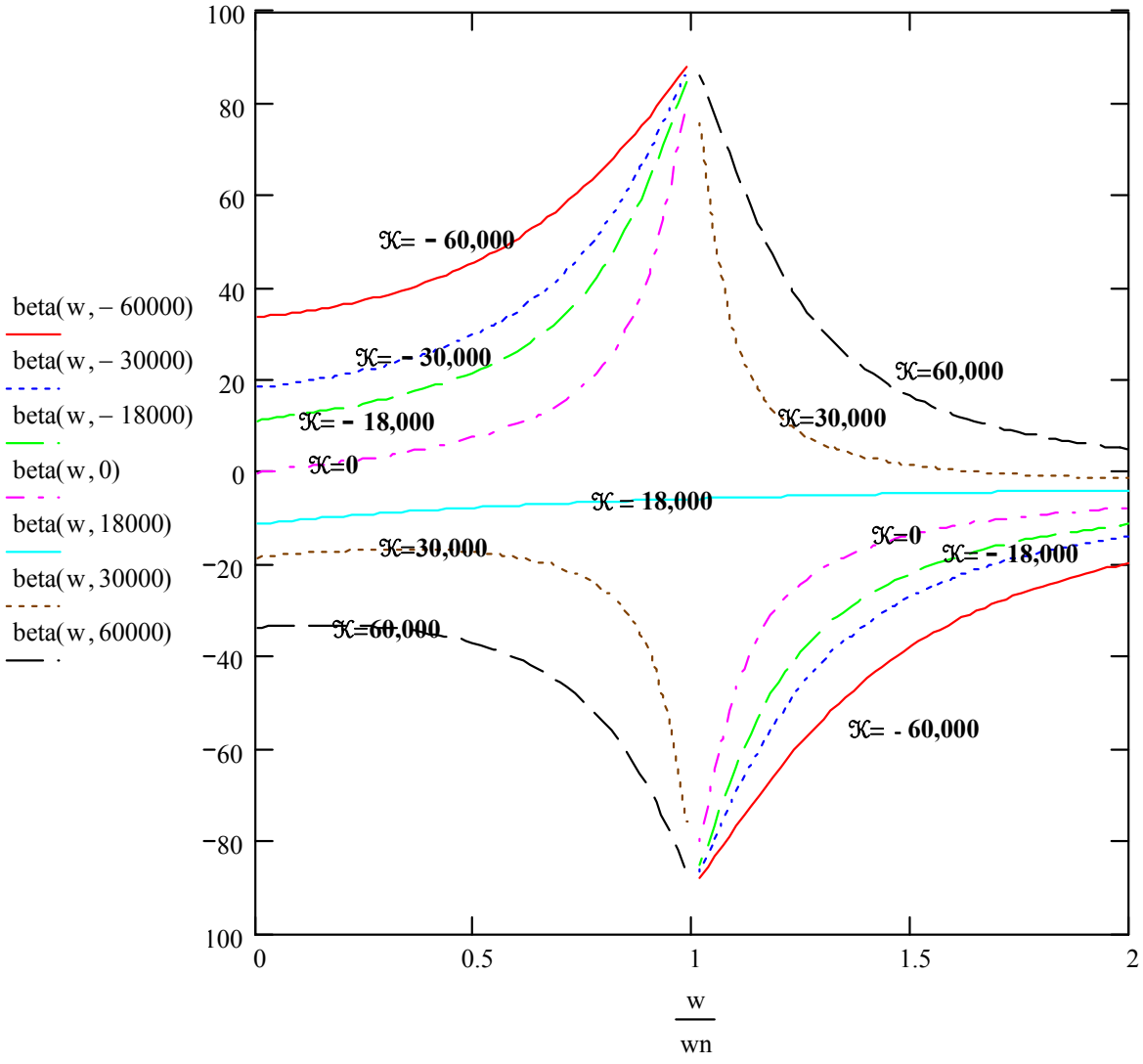

Fig 48: Plot of β against ω/ω_n for various values of cross coupled stiffness. Direct stiffness = 90000, direct damping coefficient = 10%

A typical chart is plotted in MathCAD, for a rotor with 10% damping. At speeds lower than the critical speed (for a slightly damped system) a backward driving cross coupled force increases the value of β whereas a potentially unstable forward driving cross coupling decreases β. At speeds higher than the first critical, the exact opposite occurs. Also, the change in β is most sensitive near the critical speed range. This is further illustrated in Fig 49 where the first derivative of β with respect to the cross coupled stiffness ℵ is plotted**.** The maximum change in β occurs near the critical speed range.

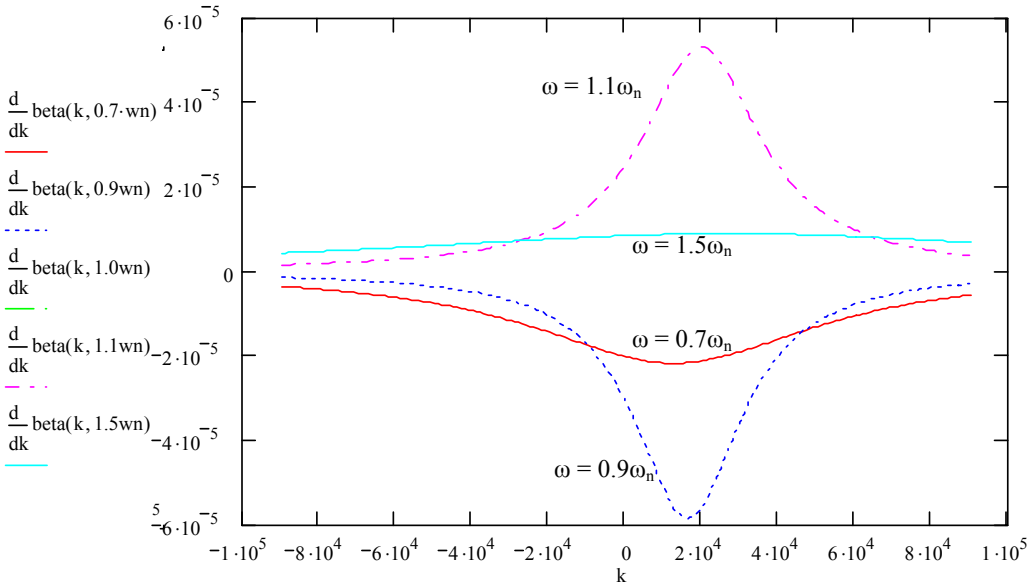

Fig 49: Plot of dβ/dℵ against ℵ at different speeds

Fig 49 also indicates that there is a definite ratio of the cross coupled stiffness to the system stiffness for which the cross coupling may have any significant effect on the system equivalent damping. In this particular case (ξ = 0.1) the ratio is 20-25%. A

similar result is presented in [1] is shown (Fig 50), where λ is the real part of the eigenvalue.

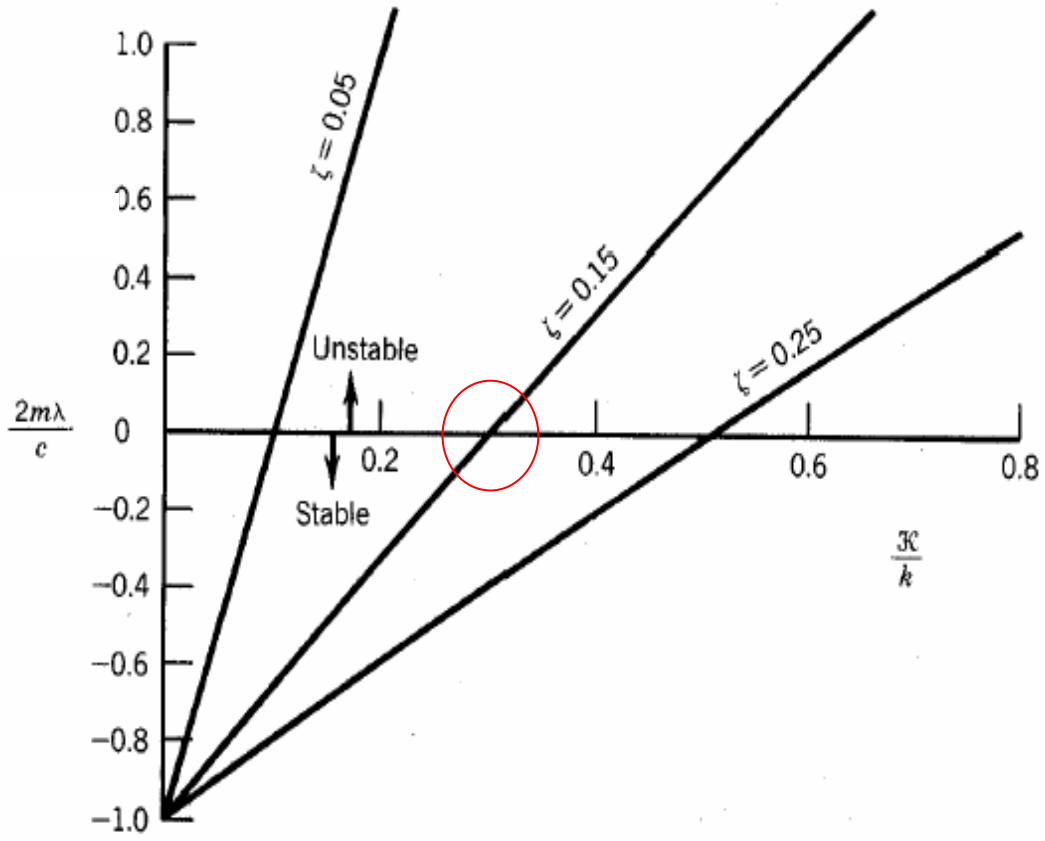

Fig 50: Effect of cross coupled stiffness on stability [1]

Synchronous Phase Angle (β)

The synchronous phase angle is the angle by which the unbalance vector leads the vibration vector in synchronous whirl (Fig 51).

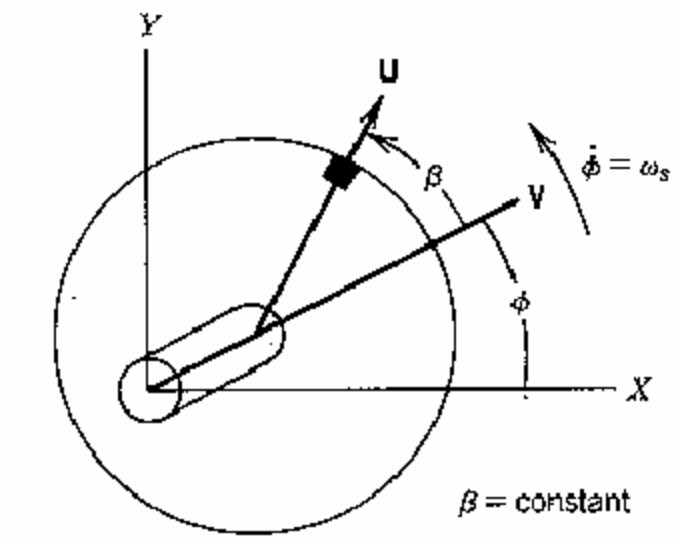

Fig 51: Synchronous phase angle β [1]

The synchronous phase angle can be measured (Fig 52) using the influence coefficient method (actual measurement of the synchronous phase angle is not required for diagnosis, but can be correlated to the phase angle displayed by most balancing instruments). The steps for measurement are detailed below:

Step 1:

Run the rotor at a particular speed 'N rpm' and save the vibration vector (1X).

$$\mathbf{V} = |\mathbf{V}| \angle \theta_1$$

All phases are measured from a fixed mark 'P' on the rotor. The 'P' mark is the exact point below the probe when the tachometer notch is lined up with the tachometer.

Step 2:

Stop the rotor and add a trial known mass at a specified angle.

$$\mathbf{M} = |\mathbf{M}| \angle \gamma$$

Step 3:

Rev the rotor up to N rpm again to find the new vibration vector

$$\mathbf{V^*} = |\mathbf{V^*}| \angle \theta_2$$

Evaluate 'β':

$$\text{Vector } \mathbf{A} = \mathbf{V^*} - \mathbf{V}$$

$$\text{Vector } \boldsymbol{\alpha} = + \mathbf{V}/\mathbf{A}$$

$$\text{Unbalance vector } \mathbf{U} = \boldsymbol{\alpha}. \mathbf{M} = |\mathbf{U}| \angle \delta$$

'β', is calculated as the angle by which the unbalance vector leads the vibration vector.

$$\text{i.e. } \boldsymbol{\beta} = \boldsymbol{\delta} - \boldsymbol{\theta_1}$$

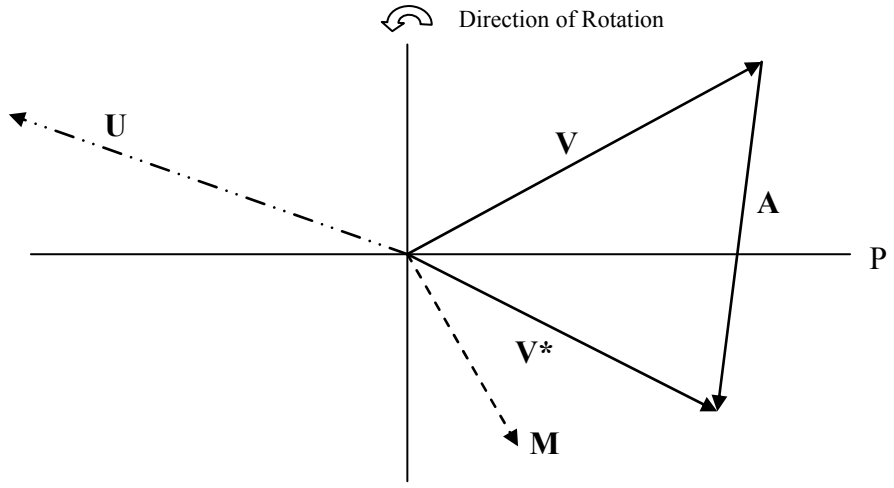

Fig 52: Measurement of the synchronous phase angle

Relationship between the Synchronous and Instrument Phase Angle

As stated earlier, the measurement of synchronous phase can be circumvented by using common industrial balancing instruments. The phase displayed by balancing

measurement instruments in the industry is however not the synchronous phase angle. A simple relationship exists between the two.

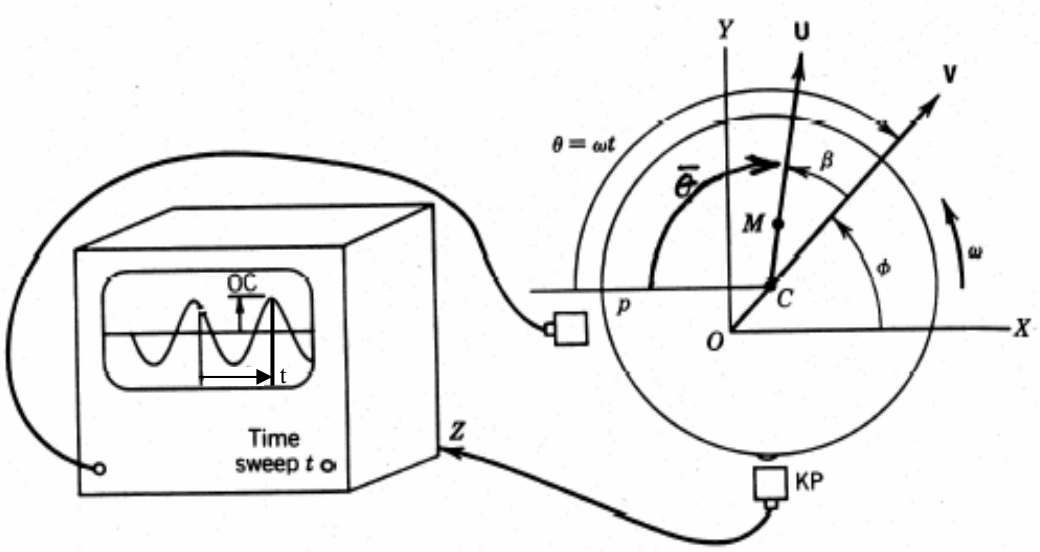

Fig 53: Instrumentation for phase measurements [1]

Fig 53 illustrates an experimental setup for phase measurements for balancing. β is the synchronous phase angle. All phase measurements in balancing machines are from the P mark on the rotor which is the exact point below the X-probe, when the tachometer notch is lined up with the tachometer. $\bar{\theta}$ is the constant angular distance of the unbalance of the rotor from the 'P' mark. All angles are measured positive opposite to the direction of rotation. Following this convention,

$$\theta = \bar{\theta} - \beta$$
$$\Delta\theta = -\Delta\beta \tag{16}$$

Experiments to Diagnose Subsynchronous Vibration

The experiment detailed below is proof of how the synchronous phase angle conclusively demarcates between instability and a benign subsynchronous vibration. The experimental rig shown in Fig 30 was used for investigating the variation of β with cross coupled instability induced from a high pressure air swirl around the rotor. A special virtual instrument was created with LabVIEW™ (Fig 54) to implement the influence coefficient method of calculating β and used in tandem with LVTRC.

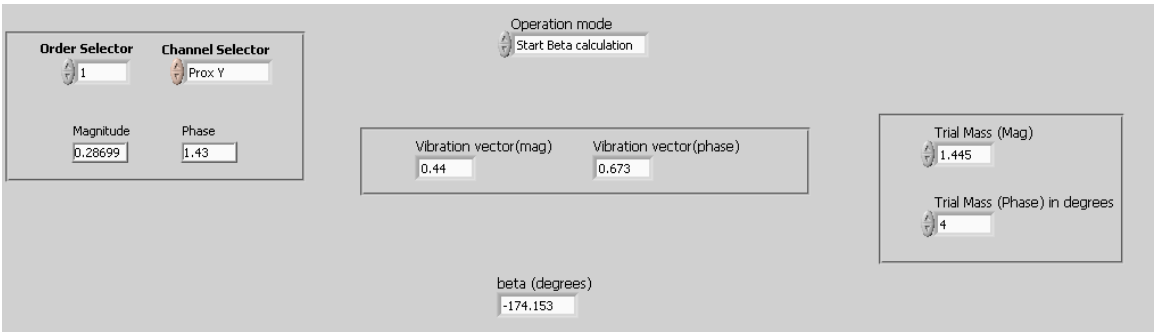

Fig 54: Virtual instrument to calculate β

Two sets of experiments were performed above the first critical speed – one with the swirl inducer turned on and one without. The frequency spectrum showed the presence of a strong subsynchronous component at the first eigenvalue in both the cases (Fig 55 and Fig 56). In the first case (Fig 55), subsynchronous vibration was induced from non-linear bearing stiffness by mounting a stiffener (as explained in Chapter V) and without air swirl around the rotor. 'β' was almost 180 degrees, as is to be expected for a lightly damped rotor. In the second case (Fig 56) the swirl inducer was pressurized at 200 psi to

induce de-stabilizing cross coupled forces (the stiffener was still mounted). The value of β increased to -174 degrees clearly showing that the subsynchronous vibration is an instability (refer to Fig 48).

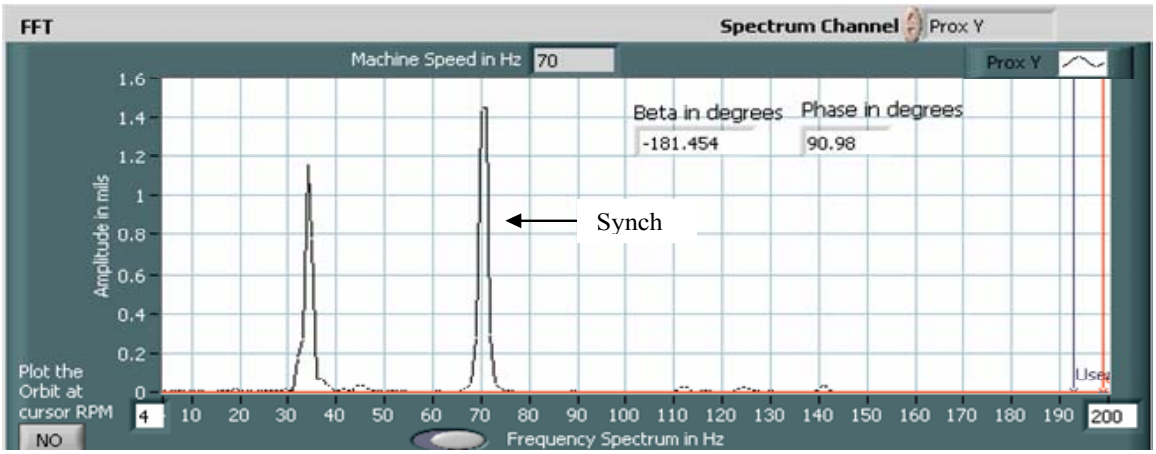

Fig 55: Benign subsynchronous vibration at 0.5X

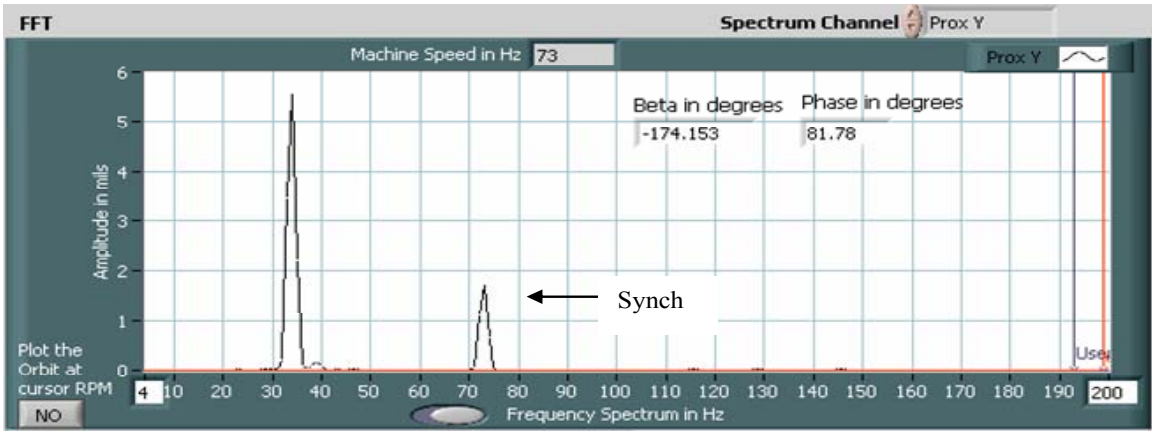

Fig 56: Unstable subsynchronous vibration at 0.5X when the swirl inducer is turned on

Note that the instrument phase shows a reverse trend and decreases from 91° to 82°. Also, $\Delta\beta$ = -7.301 degrees and $\Delta\theta$ = 9.2 degrees.

The change of phase angle from cross coupling is more pronounced near the critical speed. The experiments above were carried out at twice the critical speed so that a benign subsynchronous vibration and an instability can be compared on how they affect the phase angle. A second reason for the choice of experiment speed is that near the critical speed, with de-stabilizing cross coupling, damping is minimal. Consequently, the amplitude of vibration will be beyond safe limits. With greater direct damping (as in most industrial machines), it will be possible to carry out experiments near the critical speed. For this thesis, XLTRC simulations are used instead to study phase shifts from cross coupling in more detail for the rotor described above with higher damping.

XLTRC Simulations to Study Phase Shifts from Cross-Coupled Forces

Complete details of the XLTRC model are included in Appendix (II). Fig 57 and Fig 58 show the 'Geo plot' and the response of the rotor to unbalance excitation. De-stabilizing cross coupled forces were added to the model (Fig 59 and Fig 60) to find out how the synchronous phase angle changes.

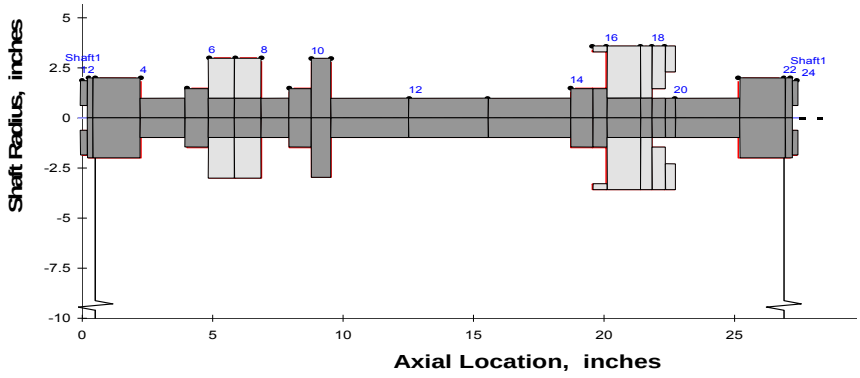

Fig 57: Geo plot of the rotor rig

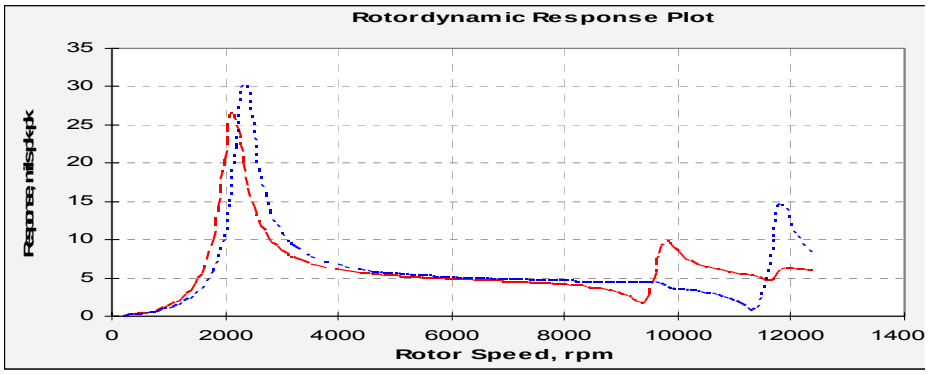

Fig 58: Response curve for the rotor

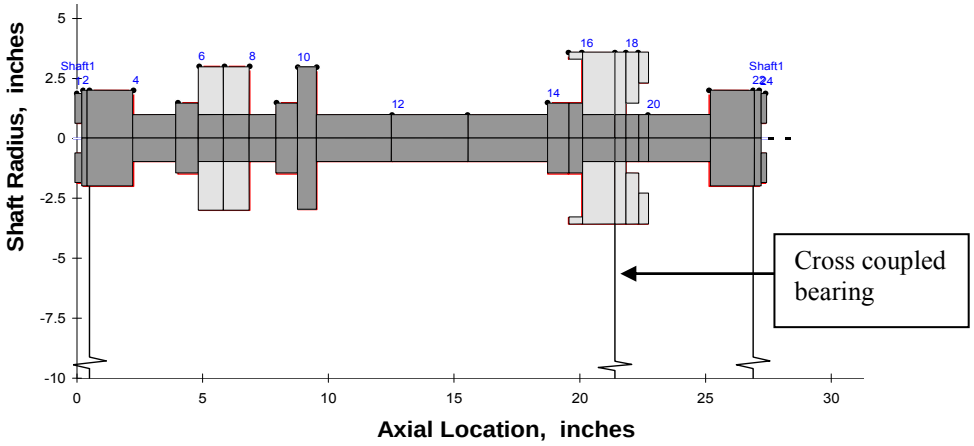

Fig 59: Rotor model with cross coupled 'bearing' at station 17

Title:	Swirl Inducer cross coupling

Perform a Paste/Special/Link for the Title box within XLTRC to create a link to your rotor model.

Speed	Kxx	Kxy	Kyx	Kyy	Cxx	Cxy	Cyx	Cyy
rpm	lb/in	lb/in	lb/in	lb/in	lb-s/in	lb-s/in	lb-s/in	lb-s/in
0		1500	-1500			0	0	
2000		1500	-1500			0	0	
4000		1500	-1500			0	0	

Fig 60: Details of the cross coupled bearing at station 17

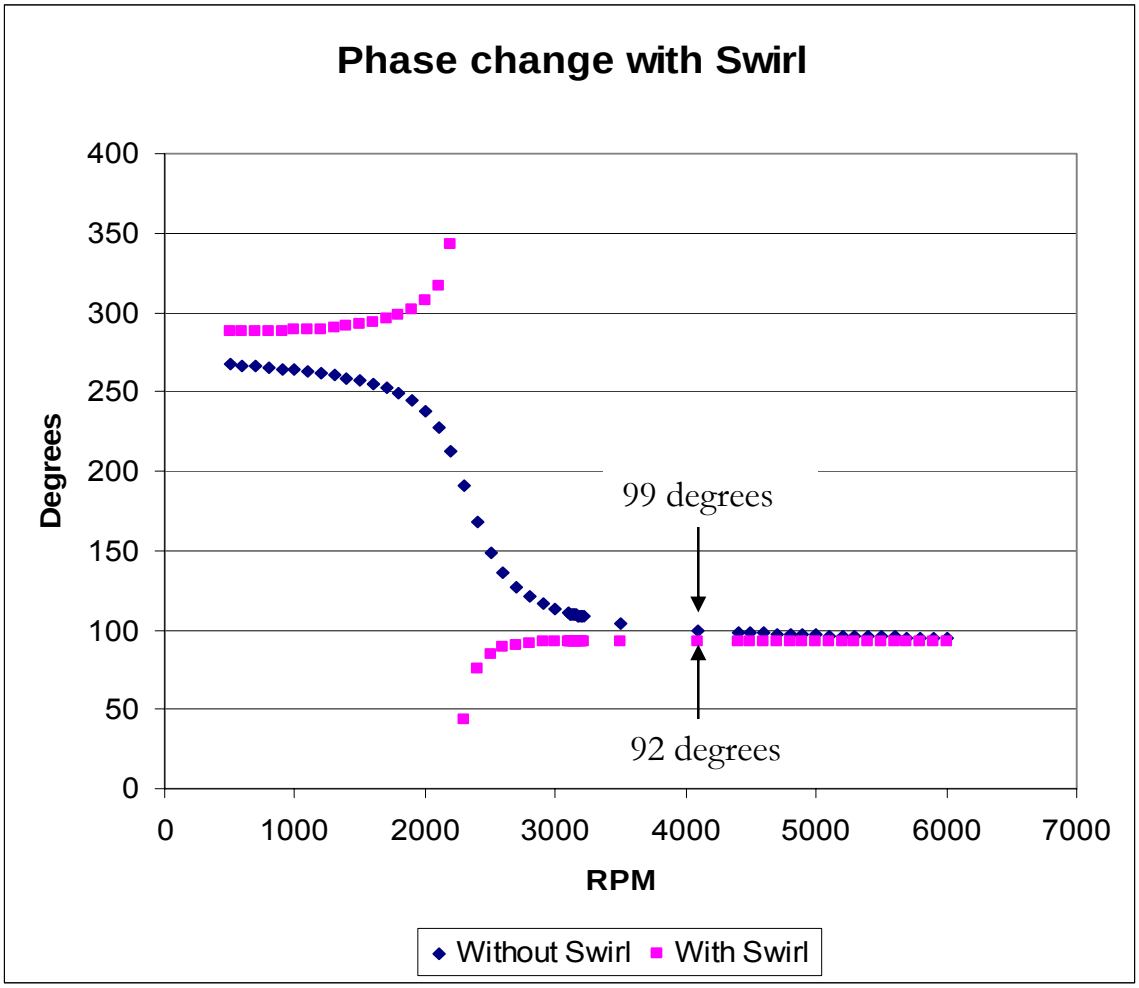

Fig 61: Instrument phase plots from XLTRC simulations with and without cross coupling

XLTRC outputs the instrument phase (not β) from the simulations and Fig 61 shows how the instrument phase changes when the cross coupling bearing is included/excluded from the model. Comparison with Fig 55 and Fig 56 show close agreement with experimental values at around 4100 RPM

Change of instrument phase from XLTRC = 99° - 92° = 7°

Change of instrument phase from actual experiments = 91° - 82° = 9°

XLTRC Simulations of the Swirl Inducer Rotor with Higher Damping

Industrial turbomachinery have much higher damping than the rotor modeled above, to decrease the vibration amplitude near the critical speed. They also require greater values of cross coupled stiffness to drive the rotor unstable. The swirl inducer model is modified to include larger direct damping at the bearings. The results follow (Fig 62, Fig 63 and Fig 64).

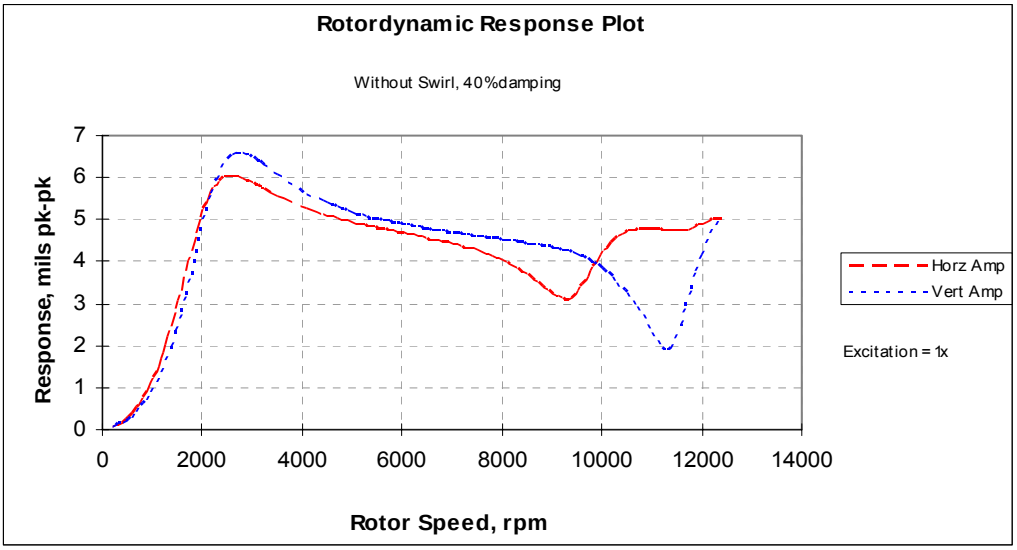

Fig 62: Response of the rotor with higher damping

Title:	Swirl Inducer cross coupling

Perform a Paste/Special/Link for the Title box within XLTRC to create a link to your rotor model.

Speed	Kxx	Kxy	Kyx	Kyy	Cxx	Cxy	Cyx	Cyy
rpm	lb/in	lb/in	lb/in	lb/in	lb-s/in	lb-s/in	lb-s/in	lb-s/in
0		4000	-4000			0	0	
2000		4000	-4000			0	0	
4000		4000	-4000			0	0	

Fig 63: Destabilizing bearing

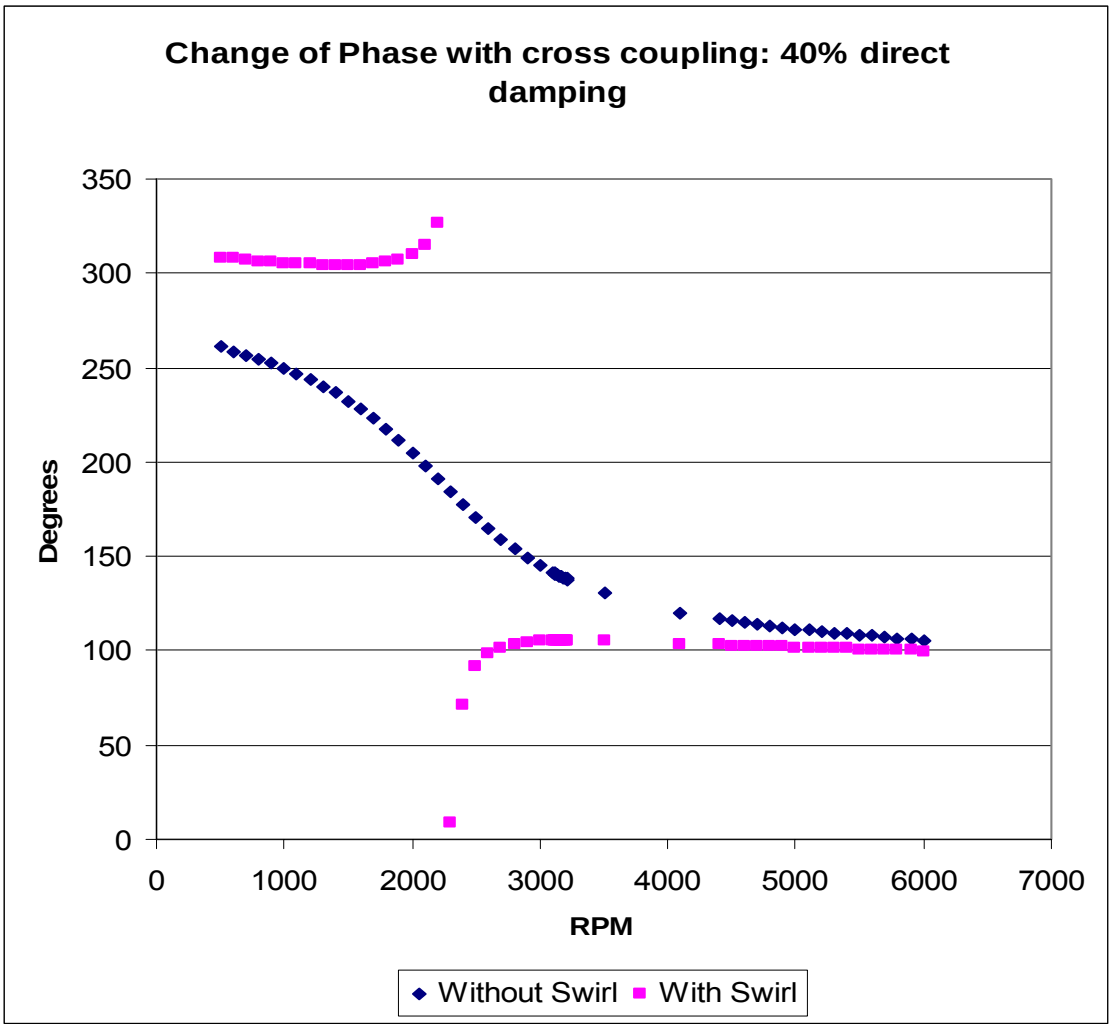

Fig 64: Change of instrument phase angle with larger direct damping

CHAPTER VII

DIAGNOSTIC INDICATORS OF BENIGN FREQUENCIES

Benign Subsynchronous Vibration and Their Indicators

Ertas, Kar and Vance [12] summarized diagnostic indicators for benign subsynchronous vibrations. Several amongst them were verified after signal analyzing vibration data from laboratory test rigs. The diagnostic indicators are discussed below:

Frequency Tracking

If the subsynchronous frequency tracks the running speed at a fixed fraction of the synchronous, then it cannot be rotordynamic instability. Of course, if the machine speed cannot be varied then tracking is impossible to determine. An exception to this rule has been observed in certain pumps where the instability tracks the synchronous at a constant fraction of around 0.8.

Agreement of Subsynchronous Frequency with known Eigenvalues of the System

Rotordynamic instability is the damped natural frequency of the rotor-bearing system. The frequency can be determined from an accurate rotordynamic model or from bump tests.

Orbit Shape – Ellipticity

The sources of most instability are de-stabilizing follower forces pushing on the rotor in the direction of subsynchronous whirl. Most follower forces are produced by cross-coupled stiffness, which models a force that is always normal to the instantaneous rotor deflection vector (orbit radius). As Fig 65 shows, this force can be purely a follower force only if the orbit is circular. The force normal to the orbit radius becomes more oblique to the orbital velocity as the orbit becomes more elliptical. The orbit shape is not an absolute indicator of potential instability. However, it can be stated that highly elliptical orbits (almost a straight line) cannot become unstable from cross-coupled stiffness.

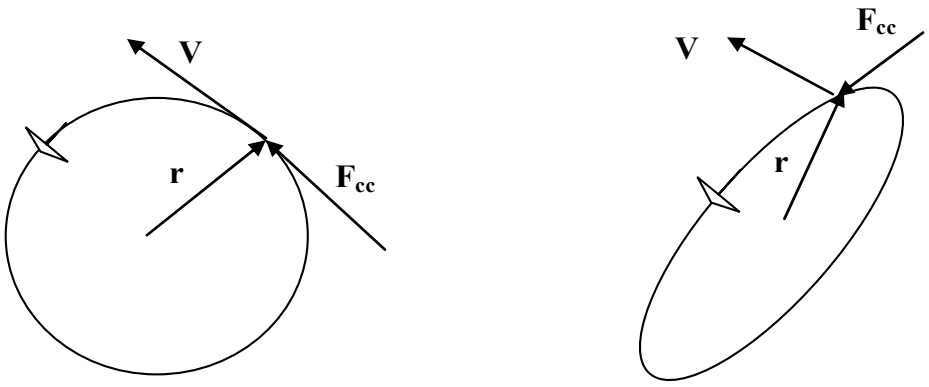

Fig 65: Cross coupled force and velocity vectors in circular and elliptical orbits

The rate of energy input to the orbit from the cross coupled force is given as,

$$J = \vec{F}_{cc}.\vec{v}$$

$$J = F_{cc} v \cos\theta$$

where, θ is the angle between the force and velocity vectors.

Since, $\cos\theta \le 1, J_{\max} = F_{cc}v$ for $\theta = 0$ i.e. for a circular orbit.

A rotor going unstable requires energy to be 'fed' into the system from the cross coupled forces in the direction of rotor whirl.

Orbits from benign subsynchronous vibrations are expected to be highly elliptical. The orbits have to be filtered at exactly the subsynchronous frequency for them to be used as any diagnostic indicator.

Presence of higher harmonics or multiple frequencies

Subsynchronous frequencies caused by loose bearing clearances, loose bearing caps, or loose foundations are excited by intermittent impact as the separated surfaces come together repeatedly as the machine runs. These impacts will excite a number of natural frequencies, not just the one of concern. Spectral analysis of the complex signal may expose a rich spectrum.

Experiments with Whirl Orbit Shapes

Two test rigs were used to capture subsynchronous orbits and test the hypothesis regarding orbit shape. The Shell rig (Fig 66) is mounted on two double row self-aligning ball bearings with a center disk constrained to the shaft. This test rig has the ability to operate with different interference fits between the center disk and the shaft. At a critical shrink fit the rotor goes violently unstable from internal friction. The Bently Rotor kit (Fig 67) was used to capture a benign subsynchronous vibration induced from the journal clearance within a worn out 'Oilite' bushing (Fig 68). LVTRC with its advanced

filtering capability was required to extract the orbits at the subsynchronous frequency desired.

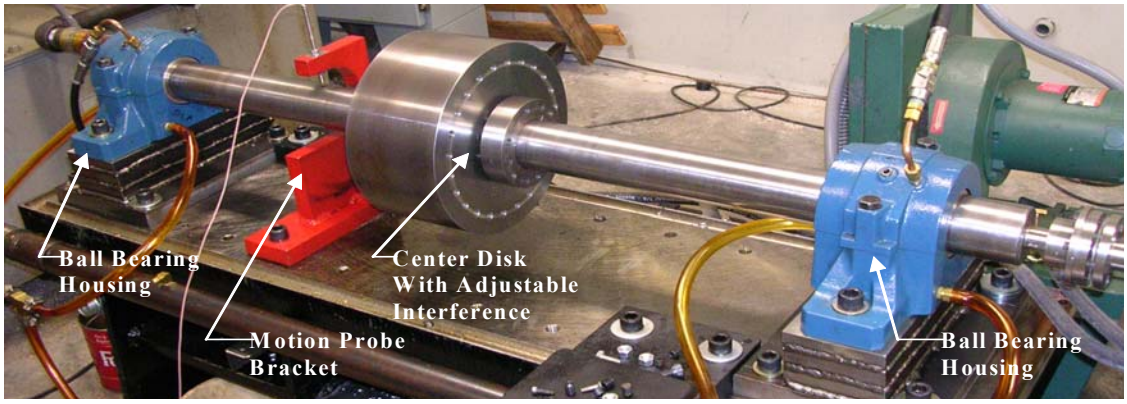

Fig 66: The Shell rotor rig

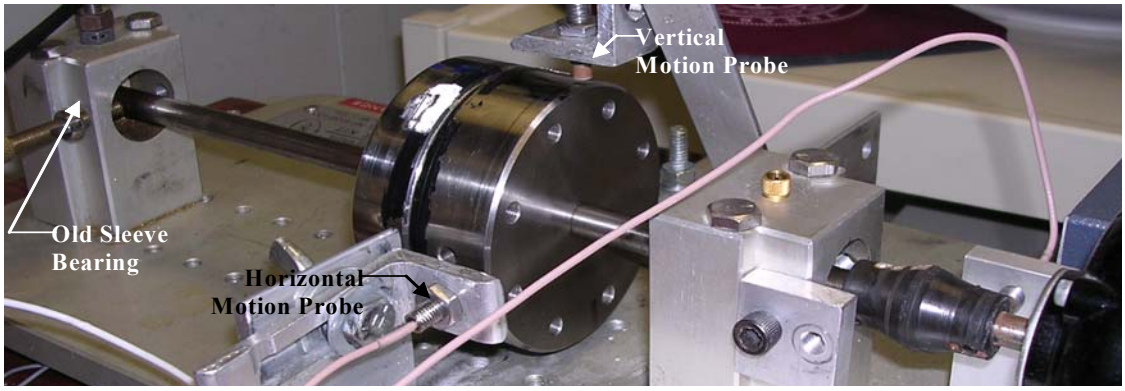

Fig 67: Bently rotor kit

Fig 68: Worn-out sleeve bearing

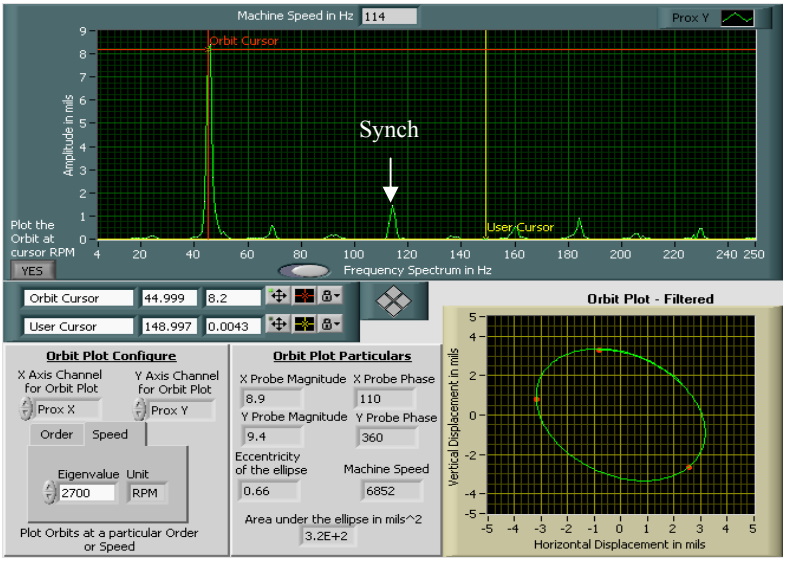

Fig 69: Almost circular unstable orbit from the Shell rotor rig

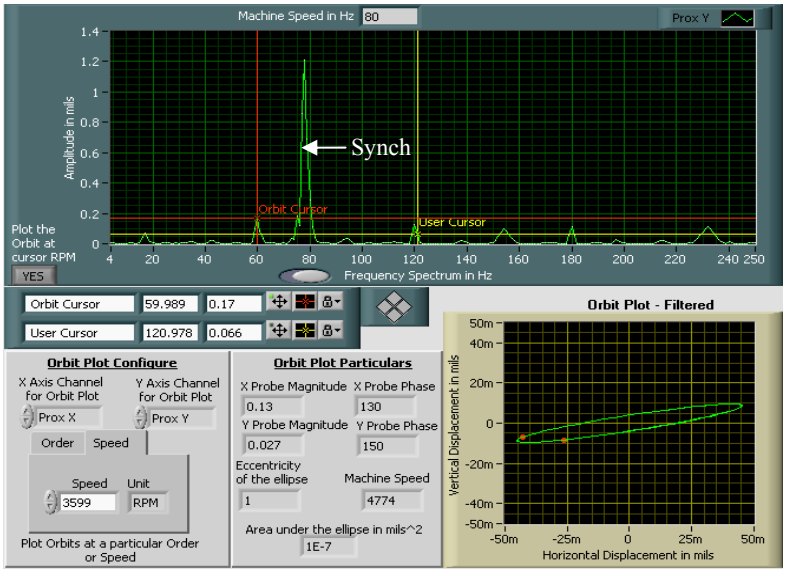

Fig 70: Benign subsynchronous orbit from the Bently rotor kit.

Fig 69 and Fig 70 show orbits from two different sources. The unstable subsynchronous orbit from the Shell rig is almost circular whereas the benign orbit is extremely elliptical.

CHAPTER VIII

CONCLUSION

This thesis has elucidated methodologies to ascertain whether a subsynchronous vibration from a rotor is potentially unstable. It has detailed vibration signatures typical to a rotating system with non-linear bearing or support stiffness, especially the large 0.5 X subharmonic response that is present when the rotor is running at twice its critical speed. The experimental results were substantiated with numerical simulations of a short rigid rotor with stiffness varying as a step function of the rotor displacement along a particular axis. The subsynchronous vibration in this case is benign, not a true instability.

A new method of diagnosing instabilities by observing changes in the synchronous phase angle was developed and verified with experiments. XLTRC simulations were also used to show that de-stabilizing cross coupling changes the synchronous phase, especially near the critical speed.

Orbit shapes were demonstrated as a potential diagnostic tool (not absolute). Highly elliptical orbits are less likely to go unstable.

As an upshot of developing advanced rotordynamic measurement and analysis tools, a state-of-the-art teststand is now available that far exceeds the capability of current market products. The teststand software – LVTRC is now in use by the Turbomachinery Research Consortium member industries.

REFERENCES

1. Vance, J.M., 1988, *Rotordynamics of Turbomachinery*, John Wiley and Sons, New York.
2. Ferrara, P.L., 1977, "Vibrations in Very High Pressure Compressors", ASME-77-DET-15.
3. Newkirk, B.L. and Taylor, H.D., 1925, "Shaft Whipping due to Oil action in Journal Bearing", General Electric Review, **28,** pp. 559-568.
4. Newkirk, B.L., 1924, "Shaft Whipping", General Electric Review, **27**, pp. 35.
5. Alford, J.S., 1964, "Protecting Turbomachinery from Self Excited Rotor Whirl", ASME-64-WA/GTP-4, pp. 333-344.
6. Den Hartog, J.P., 1956, *Mechanical Vibrations*, 4th Edition, McGraw-Hill, New York.
7. Ehrich, F.F., 1972, "Identification and Avoidance of Instabilities and Self-Excited Vibrations in Rotating Machinery", ASME-72-DE-21.
8. Ehrich, F.F., 1966, "Subharmonic Vibration of Rotors in Bearing Clearance", ASME-66-MD-1.
9. Bently, D.E., 1974, "Forced Subrotative Speed Dynamic Action of Rotating Machinery", ASME-74-PET-16.
10. Childs, D.W., 1981, "Fractional-Frequency Rotor Motion Due to Non-symmetric Clearance Effects", ASME- 81-GT-145.
11. Wachel J.C., 1982, "Rotordynamic Instability Field Problems", Rotordynamic Instability Problems in High Performance Turbomachinery -1982, NASA Conference Publication 2250, Texas A&M University, College Station.
12. Ertas, B., Kar. R, Vance J.M, 2004, "Diagnosing Subsynchronous Vibrations – Unstable or Benign", Turbomachinery Consortium Annual Report, pp. 1-55.

Supplemental sources consulted

Agilent Technologies, 2000, *The Fundamentals of Signal Analysis - Application Note 243*, Agilent Technologies, Palo Alto, California.

Ehrich, F.F., 1991, "Some Observations of Chaotic Vibration Phenomena in High Speed Rotordynamics", Journal of Vibration and Acoustics, **113**, pp. 50-57.

Ehrich, F.F., 1992, "Observations of Sub critical Super Harmonic and Chaotic Response in Rotordynamics", Journal of Vibration and Acoustics, **114**, pp. 117-121.

Eisenmann R.C, Sr., Eisenmann Robert C., Jr., 1997, *Machinery Malfunction Diagnosis and Correction*, Prentice Hall, New Jersey.

Muszynska, A., 1989 "Rotor-to-stationary Element Rub-Related Vibration Phenomena in Rotating Machinery", The Shock and Vibration Digest, **21**, pp. 3-11.

National Instruments, 2003, *LabVIEW™ Order Analysis Toolset- User Manual*, National Instruments, Austin, Texas.

www.ni.com/developer, Example codes, accessed October 2003- March 2005.

Yao-Qun Lin, 1993, "Rotor Instability Induced by Dead Band Clearance in Bearing Supports", Ph.D. Dissertation, Department of Mechanical Engineering, Texas A&M University, College Station.

APPENDIX I

Details of the LVTRC System

The NI-4472 Data Acquisition Board (courtesy: www.ni.com):

The NI 4472 is a 8-channel data acquisition device which, when used with the Sound and Vibration Toolset (LabVIEW™), allows high precision vibration measurements. The test stand uses two such boards, thus possessing the capability of 16 channel synchronized data acquisition. Input channels incorporate Integrated Electronic Piezoelectric signal conditioning for accelerometers. The channels simultaneously digitize signals over an anti-aliasing bandwidth of 0 to 45 kHz.

The NI 4472 PCI 8-Channel DSA board

Hardware

Eight analog inputs with 24 bit resolution analog-to-digital (A/D) converters achieve low noise and distortion free signals. It is possible to sample at 102.4 kilo samples / second without distortion.

Antialiasing:

Input signals are passed through fixed analog filters to remove signals with frequency

components greater than those of the ADC's; then digital antialiasing filters adjust their cut off frequency to remove any frequency components above half the sampling rate.

Multidevice synchronization:

If more than one DAQ board is used, it is necessary to synchronize their operation. Synchronization between multiboards are carried out by sharing a digital trigger from one device and synchronizing all devices to the same clock. Minimal phase mismatch is important for obtaining phase information in cross channel measurements. The NI 4472 has approximately 0.1 degree phase mismatch for a 1 kHz signal between two channels across devices.

Triggering:

Several trigger modes are available for signal acquisition. Pre-trigger mode digitizes signals before and after a trigger condition occurs. Post-trigger mode digitizes signals after a trigger condition occurs. Delay trigger mode begins signal capture after a programmable delay from the trigger. The source of the trigger can come from an analog channel or an external digital trigger input.

Calibration:

The offset voltage and gain accuracy of the analog input are calibrated by National Instruments. An onboard precision voltage reference is used for internal calibration to ensure stable, accurate DC specifications.

The SMB-120 NI Attenuation Cables:

The SMB-120 is a specific attenuation cable for the NI-447X Data acquisition boards. It has a custom attenuation circuit designed to avoid impedance mismatch and distortion.

The attenuation cable ‘weakens’ the signal by 10 dB (a gain of –10dB). The cable is designed specifically for eddy current proximity probes. By using the SMB-120 cable, both the AC and the DC components can be measured.

APPENDIX II

XLTRC^2 Model of the Experimental Rig

The following section describes in detail the geometrical characteristics and the XLTRC^2 data sheets used to model the response of the experimental rotor.

Bearing input sheets

XLUseKCM™ User Defined Support Stiffness, Damping, and Mass Rotordynamic Coefficients Press Control-F1 for help.

Version 2.0, Copyright 1996 - 1998 by Texas A&M University. All rights reserved.

Title: Swirl Inducer Bearing stiffness inducer end

Perform a Paste/Special/Link for the Title box within XLTRC to create a link to your rotor model.

Speed	Kxx	Kxy	Kyx	Kyy	Cxx	Cxy	Cyx	Cyy	Mxx	Mxy	Myx	Myy
rpm	lb/in	lb/in	lb/in	lb/in	lb-s/in	lb-s/in	lb-s/in	lb-s/in	lb-s**2/in	lb-s**2/in	lb-s**2/in	lb-s**2/in
0	2739.5	0	0	3359.9	3	0	0	3	0	0	0	0
2000	2739.5	0	0	3359.9	3	0	0	3	0	0	0	0
4000	2739.5	0	0	3359.9	3	0	0	3	0	0	0	0
5000	2739.5	0	0	3359.9	3	0	0	3	0	0	0	0

Figure II. 1: Swirl Inducer end bearing input file

XLUseKCM™ User Defined Support Stiffness, Damping, and Mass Rotordynamic Coefficients Press Control-F1 for help.

Version 2.0, Copyright 1996 - 1998 by Texas A&M University. All rights reserved.

Title: Swirl Inducer Rig Bearing at Driver end

Perform a Paste/Special/Link for the Title box within XLTRC to create a link to your rotor model.

Speed	Kxx	Kxy	Kyx	Kyy	Cxx	Cxy	Cyx	Cyy	Mxx	Mxy	Myx	Myy
rpm	lb/in	lb/in	lb/in	lb/in	lb-s/in	lb-s/in	lb-s/in	lb-s/in	lb-s**2/in	lb-s**2/in	lb-s**2/in	lb-s**2/in
0	62335	0	0	116042.3	3	0	0	3	0	0	0	0
2000	62335	0	0	116042.3	3	0	0	3	0	0	0	0
4000	62335	0	0	116042.3	3	0	0	3	0	0	0	0

Figure II. 1: Air Turbine end bearing input file

The values were obtained experimentally using a force transducer and a dial gauge.

Bearing and Seal Definitions

STN 1	STN 2	Bearing Type	UCS	UCS	Curve Type	Output	
#	#	Constraint \ Internal	Factor	Constant	Spline \ Poly	Loads	Link (*Paste Special* in here)
3	0	Constraint	1	0	Poly	no	Swirl Inducer Rig Bearing at Driver end
22	0	Constraint	1	0	Poly	no	Swirl Inducer Bearing stiffness inducer end

Figure II. 2: Bearing stations

Shaft input sheet

Shaft Properties

Shaft	Starting X_0	Starting Y_0	Int. Hyst. Damping Coeff	Int. Visc. Damping Coeff	Type of Shaft Rotation	Rotation Value	Whirl ======= Spin
#	inches	inches	η_H	η_V	Const or Ratio	rpm or N	ω / Ω
1	0	0	0	0	Ratio	1	1

Material Properties

Material	Shear Const	Axial Force Const	Density ρ	Elastic Modulus E	Shear Modulus G
#	(sc or -1)	(ax or 0)	lbm/in^3	lbf/in^2	lbf/in^2
1	-1	0	0.283	30.0E+6	12.0E+6
2	-1	0	0.1	11.5E+6	4.0E+6

Rotor Model Data Entry: Multiple Shafts, Elements, Sub-Elements and Layers.

Shaft	Element	Sub-Element	Layer	Length	Left		Right		Material	Shear Interact.	Axial Force	HIDE	Station Numbers	
					OD	ID	OD	ID					Left Station	Right Station
#	#	#	#	inches	inches	inches	inches	inches	#	(0 or 1)	lbf		#	#
1	1	1	1	0.25	3.75	1.25	3.75	1.25	1	1	0		1	2
1	2	1	1	0.25	4	0	4	0	1	1	0		2	3
1	3	1	1	1.75	4	0	4	0	1	1	0		3	4
1	4	1	1	1.77	1.94	0	1.94	0	1	1	0		4	5
1	5	1	1	0.85	2.97	0	2.97	0	1	1	0		5	6
1	6	1	1	1	1.94	0	1.94	0	1	1	0		6	layer
1	6	1	2	1	6	1.94	6	1.94	2	1	0		layer	7
1	7	1	1	1	1.94	0	1.94	0	1	1	0		7	layer
1	7	1	2	1	6	1.94	6	1.94	2	1	0		layer	8
1	8	1	1	1.07	1.94	0	1.94	0	1	1	0		8	9
1	9	1	1	0.85	2.97	0	2.97	0	1	1	0		9	10
1	10	1	1	0.75	5.93	0	5.93	0	1	1	0		10	11
1	11	1	1	3	1.94	0	1.94	0	1	1	0		11	12
1	12	1	1	3	1.94	0	1.94	0	1	1	0		12	13
1	13	1	1	3.18	1.94	0	1.94	0	1	1	0		13	14
1	14	1	1	0.83	2.97	0	2.97	0	1	1	0		14	15
1	15	1	1	0.534	7.16	6.62	7.16	6.62	2	1	0		15	layer
1	15	1	2	0.534	2.97	0	2.97	0	1	1	0		layer	16
1	16	1	1	1.315	7.16	1.94	7.16	1.94	2	1	0		16	layer
1	16	1	2	1.315	1.94	0	1.94	0	1	1	0		layer	17
1	17	1	1	0.4355	7.16	1.94	7.16	1.94	2	1	0		17	layer
1	17	1	2	0.4355	1.94	0	1.94	0	1	1	0		layer	18
1	18	1	1	0.486	7.16	2.915	7.16	2.915	2	1	0		18	layer
1	18	1	2	0.486	1.94	0	1.94	0	1	1	0		layer	19
1	19	1	1	0.3935	7.16	4.629	7.16	4.629	2	1	0		19	layer
1	19	1	2	0.3935	1.94	0	1.94	0	1	1	0		layer	20
1	20	1	1	2.43	1.94	0	1.94	0	1	1	0		20	21
1	21	1	1	1.75	4	0	4	0	1	1	0		21	22
1	22	1	1	0.25	4	0	4	0	1	1	0		22	23
1	23	1	1	0.25	3.75	1.25	3.75	1.25	1	1	0		23	24

Figure II. 3: Shaft Input

Geo Plot

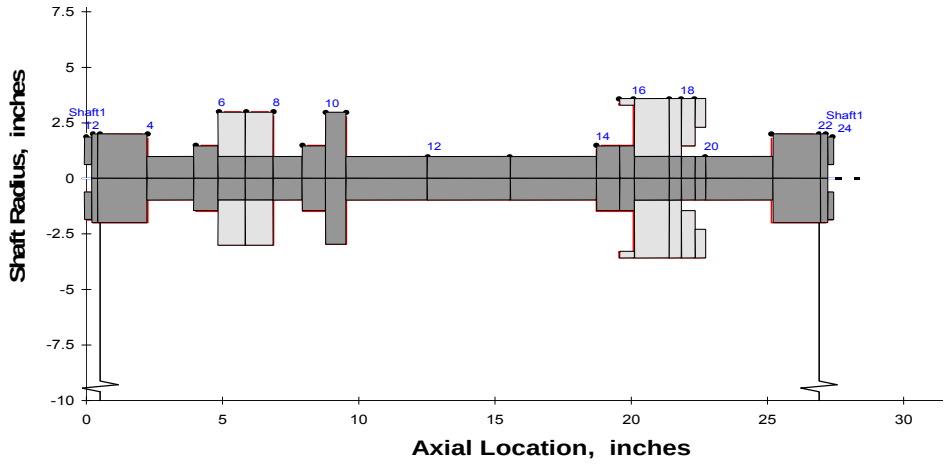

Eigenvalues

Speed	zeta1	cpm1	zeta2	cpm2	zeta3	cpm3	zeta4	cpm4	zeta5	cpm5
500.	0.118	2100.7	0.106	2327.3	0.028	9735.5	0.020	11749.6	0.022	22452.9
1000.	0.118	2100.6	0.106	2327.4	0.028	9735.3	0.020	11749.7	0.022	22450.8
1500.	0.118	2100.5	0.106	2327.5	0.028	9734.9	0.020	11750.0	0.022	22447.2
1700.	0.118	2100.4	0.106	2327.6	0.028	9734.8	0.020	11750.1	0.022	22445.4
1900.	0.118	2100.4	0.106	2327.7	0.028	9734.6	0.020	11750.2	0.022	22443.4
2000.	0.118	2100.3	0.106	2327.7	0.028	9734.5	0.020	11750.3	0.022	22442.3
2100.	0.118	2100.3	0.106	2327.8	0.028	9734.3	0.020	11750.4	0.022	22441.1
2200.	0.118	2100.2	0.106	2327.8	0.028	9734.2	0.020	11750.5	0.022	22439.9
2300.	0.118	2100.2	0.106	2327.9	0.028	9734.1	0.020	11750.6	0.022	22438.7
2500.	0.118	2100.1	0.106	2328.0	0.028	9733.8	0.020	11750.7	0.022	22436.0
3000.	0.118	2099.8	0.106	2328.3	0.028	9733.1	0.020	11751.3	0.022	22428.3
3500.	0.118	2099.4	0.106	2328.7	0.028	9732.2	0.020	11751.9	0.022	22419.3
4000.	0.118	2099.0	0.106	2329.1	0.028	9731.2	0.020	11752.6	0.022	22409.0
4500.	0.118	2098.5	0.106	2329.6	0.028	9730.0	0.020	11753.4	0.022	22397.5
6000.	0.118	2096.8	0.107	2331.4	0.028	9725.7	0.020	11756.4	0.022	22355.6
7000.	0.118	2095.4	0.107	2332.9	0.028	9722.2	0.020	11758.9	0.022	22322.2
8000.	0.118	2093.8	0.107	2334.6	0.028	9718.1	0.020	11761.7	0.022	22284.8
9000.	0.118	2092.0	0.107	2336.5	0.028	9713.5	0.020	11764.9	0.022	22243.7
10000.	0.118	2090.1	0.107	2338.5	0.028	9708.4	0.020	11768.4	0.022	22199.4

Figure II. 5: Damped Natural Frequency

Mode shapes

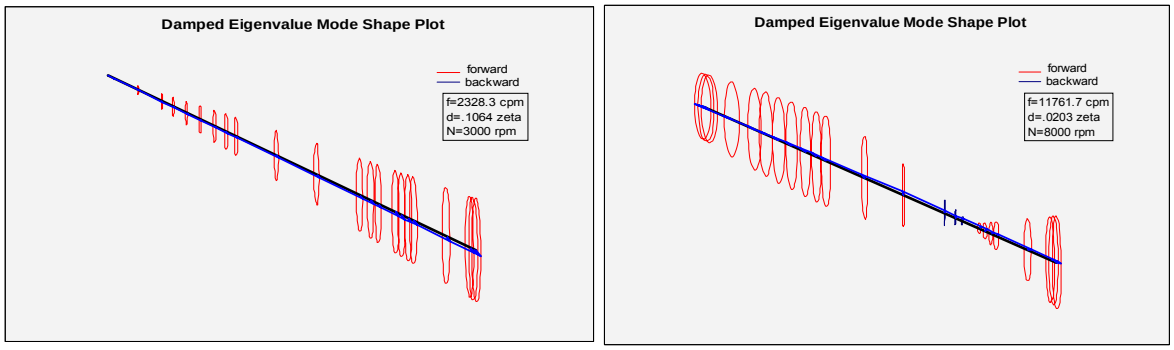

Figure II. 6: 1st and 2nd Forward Mode shapes

Response

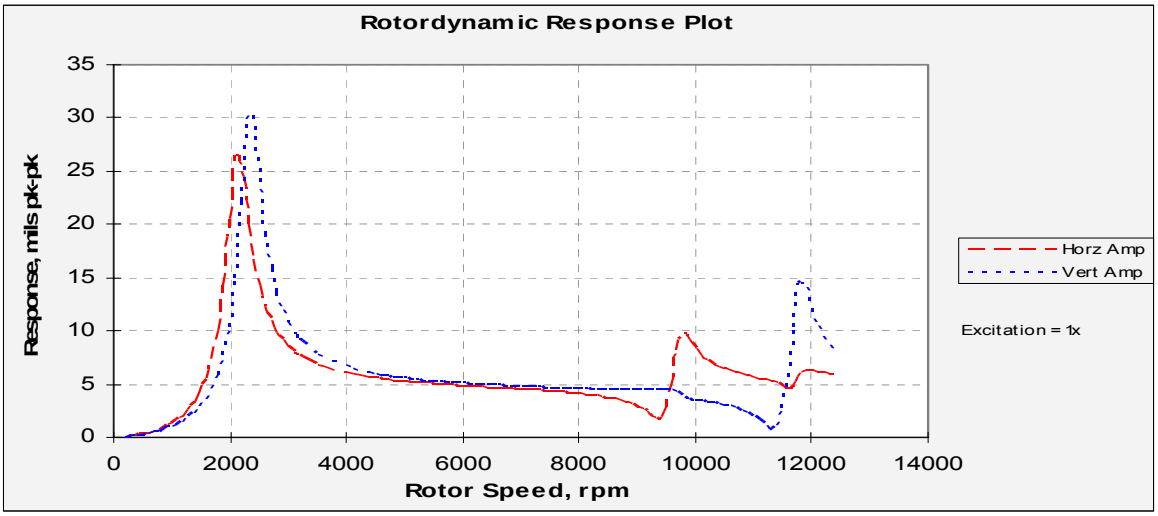

Figure II. 7: Response to 1X excitation

De-stabilizing Cross Coupled Forces to drive the Rotor unstable

De-stabilizing cross coupled forces were added to the XLTRC model to find out how the synchronous phase angle changes.

Title:	Swirl Inducer cross coupling

Perform a Paste/Special/Link for the Title box within XLTRC to create a link to your rotor model.

Speed	Kxx	Kxy	Kyx	Kyy	Cxx	Cxy	Cyx	Cyy
rpm	lb/in	lb/in	lb/in	lb/in	lb-s/in	lb-s/in	lb-s/in	lb-s/in
0		1500	-1500			0	0	
2000		1500	-1500			0	0	
4000		1500	-1500			0	0	

Figure II. 8: Bearing model for Destabilizing cross coupled forces

Bearing and Seal Definitions							
STN 1	STN 2	Bearing Type	UCS	UCS	Curve Type	Output	Link (*Paste Special* in here)
#	#	Constraint \ Internal	Factor	Constant	Spline \ Poly	Loads	
3	0	Constraint	1	0	Poly	no	Swirl Inducer cross coupling
22	0	Constraint	1	0	Poly	no	Swirl Inducer Bearing stiffness inducer end
17	0	Constraint	1	0	Poly	no	Swirl Inducer cross coupling

Figure II. 9: Inclusion of the bearing at station 17 (Swirl inducer)

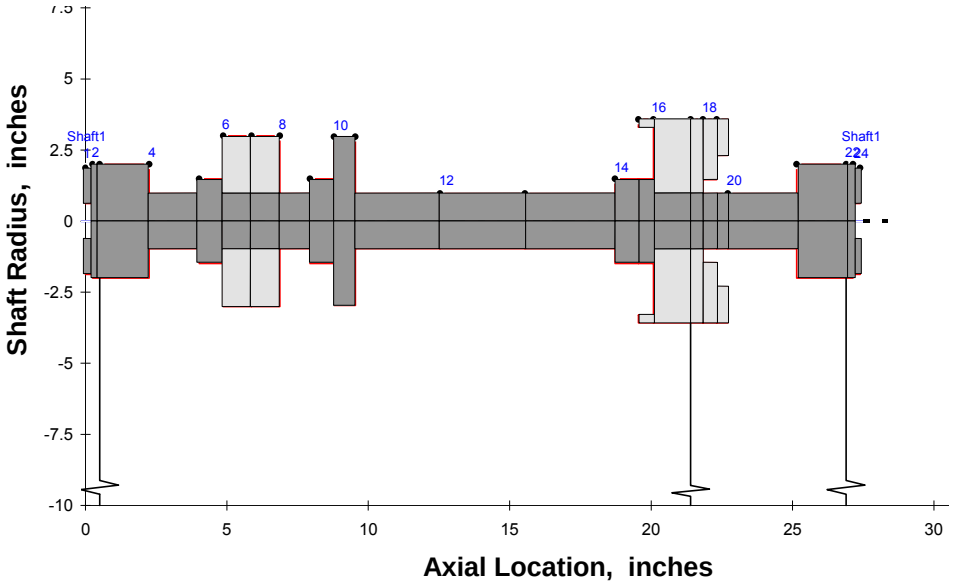

Figure II. 10: Modified Geo Plot

Speed	zeta1	cpm1	zeta2	cpm2	zeta3	cpm3	zeta4	cpm4
500.	-0.033	2313.1	0.598	2365.0	0.094	9662.1	0.066	11656.6
1000.	-0.033	2315.3	0.598	2361.7	0.094	9661.0	0.066	11657.8
1500.	-0.032	2317.5	0.599	2358.4	0.094	9659.8	0.065	11659.0
1700.	-0.032	2318.4	0.599	2357.1	0.094	9659.3	0.065	11659.5
1900.	-0.032	2319.2	0.599	2355.8	0.094	9658.7	0.065	11660.0
2000.	-0.032	2319.7	0.599	2355.1	0.094	9658.4	0.065	11660.3
2100.	-0.032	2320.1	0.599	2354.5	0.094	9658.2	0.065	11660.6
2200.	-0.032	2320.6	0.600	2353.8	0.094	9657.9	0.065	11660.8
2300.	-0.032	2321.0	0.600	2353.2	0.094	9657.6	0.065	11661.1
2500.	-0.031	2321.9	0.600	2351.9	0.095	9657.0	0.065	11661.7
3000.	-0.031	2324.1	0.600	2348.6	0.095	9655.4	0.065	11663.1
3500.	-0.031	2326.3	0.601	2345.3	0.095	9653.6	0.064	11664.7
4000.	-0.030	2328.5	0.601	2342.0	0.095	9651.8	0.064	11666.3
4500.	-0.030	2330.7	0.602	2338.7	0.095	9649.8	0.064	11668.1
6000.	-0.028	2337.4	0.603	2328.9	0.095	9643.1	0.063	11673.8

Figure II. 11: Eigenvalue Table showing that the first forward mode is unstable

Speed rpm	Horz Amp mils pk-pk	Horz Phs degrees	Vert Amp mils pk-pk	Vert Phs degrees
200	0.038941	89.12254	0.031744	359.2864
300	0.088593	88.6693	0.07207	358.9201
400	0.159992	88.1979	0.12977	358.5419
500	0.255181	87.70101	0.206167	358.1474
600	0.377029	87.16996	0.303091	357.7311
700	0.529463	86.59429	0.422993	357.287
800	0.717802	85.96088	0.569105	356.8077
900	0.949275	85.25283	0.745677	356.2841
1000	1.233794	84.44778	0.958317	355.7047
1100	1.585177	83.51519	1.214487	355.055
1200	2.023106	82.41207	1.52425	354.3156
1300	2.576398	81.07569	1.901412	353.4607
1400	3.288695	79.41075	2.365322	352.4548
1500	4.228803	77.26532	2.94381	351.2481
1600	5.510398	74.38287	3.678176	349.7687
1700	7.331096	70.29928	4.632076	347.9114
1800	10.04868	64.10498	5.908813	345.5211
1900	14.28696	53.87962	7.691393	342.3664
2000	20.61637	35.69407	10.37023	337.974
2100	26.21211	5.933501	14.88441	330.184
2200	24.50698	335.4161	22.13681	313.7107
2300	19.99079	316.9228	29.988	285.2
2400	16.76416	305.3876	30.24526	251.2452
2500	14.23562	297.1955	24.37293	227.521
2600	12.32936	291.8968	19.27838	214.2325
2700	10.94585	288.3693	15.85801	206.4886
2800	9.922806	285.8687	13.55771	201.5702
2900	9.143443	284.0011	11.94416	198.2071
3000	8.533004	282.5497	10.76332	195.7728
3100	8.04341	281.3867	9.867462	193.9318
3110	7.99977	281.2829	9.789773	193.7721
3120	7.956987	281.1811	9.71395	193.6162
3130	7.915037	281.0812	9.639927	193.464
3140	7.873895	280.9832	9.567645	193.3153
3150	7.833542	280.887	9.497045	193.1701
3160	7.793953	280.7926	9.42807	193.0281
3170	7.755109	280.7	9.360668	192.8893
3180	7.716989	280.609	9.294787	192.7536
3190	7.679573	280.5196	9.23038	192.6209
3200	7.642845	280.4319	9.167398	192.491
3210	7.606782	280.3456	9.105794	192.364
3220	7.571372	280.2609	9.045529	192.2396
3500	6.787941	278.3647	7.768417	189.5803
4100	5.860889	276.0136	6.392496	186.5947
4400	5.582558	275.2634	6.008859	185.7106
4500	5.505434	275.05	5.905271	185.4651
4600	5.434475	274.8513	5.811113	185.2389
4700	5.368912	274.6655	5.725162	185.0295
4800	5.308092	274.4913	5.64639	184.835
4900	5.251444	274.3273	5.573933	184.6536
5000	5.198482	274.1725	5.507051	184.4838
5100	5.148777	274.0259	5.44511	184.3245
5200	5.101954	273.8867	5.387565	184.1745
5300	5.057681	273.7541	5.333945	184.0328
5400	5.015662	273.6276	5.283836	183.8987
5500	4.975633	273.5066	5.236881	183.7714
5600	4.937354	273.3905	5.192759	183.6503
5700	4.900608	273.2788	5.151194	183.5348
5800	4.865195	273.1713	5.111936	183.4245
5900	4.830928	273.0675	5.074763	183.3188
6000	4.797633	272.967	5.039479	183.2174

Figure II. 12: Response without cross coupling

Speed rpm	Horz Amp mils pk-pk	Horz Phs degrees	Vert Amp mils pk-pk	Vert Phs degrees
200	0.036677	15.42908	0.03049	289.0259
300	0.083548	14.96375	0.069438	288.7151
400	0.151005	14.53617	0.125406	288.4732
500	0.240927	14.1429	0.199832	288.3012
600	0.355911	13.78094	0.294685	288.2018
700	0.499445	13.44776	0.412611	288.1794
800	0.676188	13.14124	0.557142	288.241
900	0.892354	12.85973	0.733008	288.3959
1000	1.15629	12.60219	0.946616	288.6573
1100	1.479345	12.36852	1.206786	289.0424
1200	1.877202	12.1602	1.525939	289.5741
1300	2.372	11.98162	1.922067	290.2824
1400	2.995814	11.84281	2.422147	291.2065
1500	3.796689	11.76489	3.068333	292.3976
1600	4.849624	11.79186	3.929785	293.9241
1700	6.278337	12.01579	5.126706	295.8825
1800	8.30269	12.63431	6.883299	298.4292
1900	11.35646	14.09199	9.657573	301.886
2000	16.42958	17.48213	14.5113	307.1082
2100	26.23477	26.01073	24.36677	316.9573
2200	47.84711	51.85514	47.13383	343.2533
2300	54.77171	112.132	57.28316	42.913
2400	32.29723	145.7341	35.59097	74.91663
2500	21.46615	158.0882	24.59095	85.03119
2600	16.19907	164.4869	19.00596	88.96626
2700	13.22715	168.6188	15.69316	90.73617
2800	11.36396	171.577	13.50932	91.61043
2900	10.10418	173.7948	11.96598	92.07722
3000	9.202317	175.4961	10.82128	92.34586
3100	8.527245	176.8202	9.941543	92.51224
3110	8.469003	176.9358	9.86475	92.52529
3120	8.4122	177.0487	9.789724	92.53781
3130	8.35678	177.1589	9.716402	92.54985
3140	8.302697	177.2666	9.644734	92.56142
3150	8.249902	177.3717	9.574666	92.57256
3160	8.198351	177.4744	9.506144	92.58328
3170	8.147998	177.5748	9.439123	92.59361
3180	8.098805	177.6729	9.373556	92.60356
3190	8.05073	177.7687	9.309397	92.61316
3200	8.003738	177.8623	9.246602	92.62242
3210	7.957788	177.9538	9.185133	92.63135
3220	7.912852	178.0432	9.124947	92.63997
3500	6.961244	179.8918	7.838603	92.79678
4100	5.921533	181.5954	6.43443	92.88024
4400	5.623178	181.947	6.041319	92.86048
4500	5.541418	182.0264	5.935178	92.84815
4600	5.46652	182.0917	5.838716	92.83345
4700	5.397589	182.1447	5.750685	92.81665
4800	5.333865	182.1874	5.670037	92.79798
4900	5.274705	182.2212	5.59588	92.77763
5000	5.219554	182.2472	5.527456	92.75579
5100	5.167935	182.2665	5.464117	92.73261
5200	5.119429	182.28	5.405299	92.70823
5300	5.073672	182.2883	5.35052	92.68278
5400	5.030341	182.2922	5.299356	92.65638
5500	4.989146	182.2922	5.251434	92.62911
5600	4.949829	182.2887	5.206428	92.60106
5700	4.912156	182.2823	5.164053	92.57232
5800	4.875915	182.2732	5.124052	92.54296
5900	4.840907	182.2618	5.086197	92.51302
6000	4.806951	182.2484	5.050288	92.48257

Figure II. 13: Response with cross coupling

VITA

Name:	Rahul Kar
Address:	Department of Mechanical Engineering, 3123, TAMU, College Station, Texas, USA.
Email:	kar.rahul@gmail.com
Education:	B.E., Mechanical Engineering, National Institute of Technology, India, 2002 M.S., Mechanical Engineering, Texas A&M University, USA, 2005